Monthly Notices
of the
ROYAL ASTRONOMICAL SOCIETY

Mon. Not. R. Astron. Soc. **403,** 569–588 (2010) doi:10.1111/j.1365-2966.2009.16074.x

Polarization changes of pulsars due to wave propagation through magnetospheres

Chen Wang,[1,2]★ Dong Lai[2] and JinLin Han[1]★

[1]*National Astronomical Observatories, Chinese Academy of Sciences. A20 Datun Road, Chaoyang District, Beijing 100012, China*
[2]*Department of Astronomy, Cornell University, Ithaca, NY 14853, USA*

Accepted 2009 November 19. Received 2009 November 18; in original form 2009 October 7

ABSTRACT

We study the propagation effects of radio waves in a pulsar magnetosphere, composed of relativistic electron–positron pair plasmas streaming along the magnetic field lines and corotating with the pulsar. We critically examine the various physical effects that can potentially influence the observed wave intensity and polarization, including resonant cyclotron absorption, wave mode coupling due to pulsar rotation, wave propagation through quasi-tangential regions (where the photon ray is nearly parallel to the magnetic field) and mode circularization due to the difference in the electron/positron density/velocity distributions. We numerically integrate the transfer equations for wave polarization in the rotating magnetosphere, taking account of all the propagation effects in a self-consistent manner. For typical magnetospheric plasma parameters produced by pair cascade, we find that the observed radio intensity and polarization profiles can be strongly modified by the propagation effects. For a relatively large impact parameter (the minimum angle between the magnetic dipole axis and the line of sight), the polarization angle profile is similar to the prediction from the Rotating Vector Model, except for a phase shift and an appreciable circular polarization. For a smaller impact parameter, the linear polarization position angle may exhibit a sudden 90° jump due to the quasi-tangential propagation effect, accompanied by a complex circular polarization profile. Some applications of our results are discussed, including the origin of non-Gaussian pulse profiles, the relationship between the position angle profile and circular polarization in conal-double pulsars, and the orthogonal polarization modes.

Key words: plasmas – polarization – waves – stars: magnetic fields – pulsars: general.

1 INTRODUCTION

Pulsar radio emission is likely generated within a few hundred kilometres from the neutron star (NS) surface (e.g. Cordes 1978; Blaskiewicz, Cordes & Wasserman 1991; Kramer et al. 1997; Kijak & Gil 2003). A pulsar is surrounded by a magnetosphere filled with relativistic electron–positron pair plasmas (plus possibly a small number of ions) within the light cylinder. When radio waves propagate through the magnetosphere, the total flux, polarization state and spectrum of the emission may be modified by propagation effects. Understanding the property of wave propagation in pulsar magnetospheres is necessary for the interpretation of various observations of pulsars.

Radio emission from pulsars shows strong linear polarization (LP). For some pulse components or even the whole pulse profiles, it can be 100 per cent polarized (e.g. Lyne & Manchester 1988; Gould & Lyne 1998; Weisberg et al. 1999, 2004; Han et al. 2009). LP is closely related to magnetic field lines where the emission was generated. Based on the linear polarization position angle (PA) curve of Vela pulsar, the Rotating Vector Model (RVM) was suggested by Radhakrishnan & Cooke (1969). For some pulsars, especially the so-called conal-double-type pulsars, RVM works very well (e.g. Mitra & Li 2004). However, the PA curves of most pulsars are much more complex and do not follow the simple RVM. The deviation from the RVM could be caused by the intrinsic emission mechanism (e.g. Blaskiewicz et al. 1991), which is highly uncertain (e.g. Lyubarsky 2008), and/or the propagation effect through the pulsar magnetosphere (see below). Also, the PA curves or polarization observations of individual pulses show the orthogonal polarization mode (OPM) phenomenon, in which the polarization position angle exhibits a sudden ∼ 90° jump (e.g. Manchester, Taylor & Huguenin 1975; Backer, Rankin & Campbell 1976;

★E-mail: cwang@astro.cornell.edu (CW), dong@astro.cornell.edu (DL), hjl@nao.cas.cn (JLH)

Cordes, Rankin & Backer 1978; Stinebring et al. 1984a,b; Xilouris et al. 1995). It is not clear whether the OPM arises from the emission process (e.g. Luo & Melrose 2004) or the propagation effect (e.g. McKinnon & Stinebring 2000).

Another important observational feature of pulsar radio emission is the circular polarization (CP; e.g. Rankin 1983; Radhakrishnan & Rankin 1990; Han et al. 1998). Significant CPs have been observed in individual pulses of pulsars with mean values of typically 20–30 per cent. Very high degrees of CP are occasionally observed from some components of pulsar profiles (e.g. Cognard et al. 1996; Han et al. 2009). Radhakrishnan & Rankin (1990) identified two main types of CP signature: antisymmetric type with sign reverse in the mid-pulse and symmetric type without sign change over the whole profile. They concluded that the CP of the antisymmetric type is associated with the core emission and strongly correlated with the sense of rotation of the linear position angle. Han et al. (1998) showed that this correlation is not kept for a larger sample, and they found that for conal-double pulsars the sense of CP is correlated with the sense of PA curves.

The diverse behaviours of pulsar polarization (including LP and CP) may require more than one mechanism for proper explanations. First, they may be caused by an intrinsic mechanism in the emission region and/or process. For example, Radhakrishnan & Rankin (1990) suggested that geometrical effect on the pulsar beam from curvature radiation can naturally generate antisymmetric CP for the core components. Gangadhara (1997) suggested that the observed CP could be caused by the coherent superposition of two orthogonal modes emitted by positrons and electrons. Xu et al. (2000) interpreted the CP by the superposition of coherent inverse Compton scattering. Kazbegi, Machabeli & Melikidze (1991) suggested that cyclotron instability may be responsible for the circular polarization. Also, Luo & Melrose (2001) suggested that circular polarization can develop by cyclotron absorption when the distributions (especially the number densities) of the magnetospheric electrons and positrons are different.

However, many observed characteristics of the pulsar radio emission are most likely dictated by the wave propagation in the magnetospheric plasma (see e.g. Melrose 2003; Lyubarsky 2008 for a review). A number of theoretical works have been devoted to study how magnetosphere propagation influences pulsar polarization observations. Whatever the emission mechanism, radio wave propagates in the plasma in the form of two orthogonally polarized normal modes. The polarization state of the wave evolves along the ray, following the direction of the local magnetic field, a process termed 'adiabatic walking' (Cheng & Ruderman 1979). Cheng & Ruderman (1979) introduced two propagation effects: the wave mode coupling effect for a pure pair plasma and the circularization effect (natural modes become circular polarized), both of which can generate circular polarization. Melrose (1979) and Allen & Melrose (1982) suggested that the separation of natural waves (because of different refractive indices) can cause the OPM phenomenon. Arons & Barnard (1986) studied the wave dispersion relation and natural modes in the relativistic pair plasma. Lyubarskii & Petrova (1998) considered the natural modes in a relativistic plasma with corotating velocity in the infinite magnetic field limit, and Petrova & Lyubarskii (2000) studied refraction and polarization transfer in such a plasma. Luo & Melrose (2001) and Fussell, Luo & Melrose (2003) studied the cyclotron absorption of radio emission within pulsar magnetospheres. Petrova (2006) further studied the polarization transfer in pulsar magnetosphere and considered the wave mode coupling and cyclotron absorption effect. Johnston et al. (2005) suggested that the variation of circular polarization of PSR B1259−63 during the ellipse with its main-sequence companion is related to the wave propagation effect in the magnetosphere of the companion star. However, none of the previous studies has calculated the final polarization profiles with all of these propagation effects included in a self-consistent way within a single theoretical framework. It is often unclear which of the effects are most important, and if so, under what conditions. In this paper, we attempt to combine all the propagation effects, evaluate their relative importance and use numerical integration along the photon ray to study the influence of propagation effects on the final polarization states.

This paper is organized as follows. In Section 2, we present the geometrical model for our calculation and the general wave evolution equation in a magnetized plasma. In Section 3, we give the expression of the dielectric tensor of a relativistic pair plasma characterizing the magnetosphere of a pulsar and discuss the natural wave modes and their evolution. In Section 4, we study several important propagation effects separately: cyclotron absorption, wave mode coupling, circularization and the quasi-tangential (QT) propagation (see Wang & Lai 2009). In Section 5, we present numerical calculations of the single photon evolution and the phase profiles of pulsar emission beam. Our results and possible applications are presented in Section 6.

2 GEOMETRY AND GENERAL WAVE EVOLUTION EQUATION

2.1 Geometrical model

Consider a photon (radio wave) emitted at the initial position $\boldsymbol{r}_{\rm i}$ at time $t_{\rm i}$ (corresponding to the pulsar rotation phase $\Psi_{\rm i}$). Suppose the photon trajectory is a straight line along $\boldsymbol{k}$ (the wave vector). In a fixed XYZ frame with $\hat{\boldsymbol{Z}} = \hat{\boldsymbol{k}}$ along the line of sight and $\boldsymbol{\Omega}$ (the pulsar spin vector) in the XZ plane ($\hat{\boldsymbol{Z}} \times \hat{\boldsymbol{\Omega}} = \sin\zeta\,\hat{\boldsymbol{Y}}$, where ζ is the angle between $\boldsymbol{k}$ and $\boldsymbol{\Omega}$; see Fig. 1), the photon position after emission and the corresponding pulsar rotation phase are

$$\boldsymbol{r} = \boldsymbol{r}_{\rm i} + s\hat{\boldsymbol{Z}}, \tag{2.1}$$

$$\Psi = \Psi_{\rm i} + \Omega(t - t_i) = \Psi_{\rm i} + s/r_{\rm lc}, \tag{2.2}$$

where $s = c(t - t_{\rm i})$ is the distance from the emission point along the ray and $r_{\rm lc} = c/\Omega$ the radius of the light cylinder. The rotating magnetic field is given by

$$\boldsymbol{B}(s) = -\nabla(\boldsymbol{\mu}\cdot\boldsymbol{r}/r^3) = -\frac{\boldsymbol{\mu}}{r^3} + \frac{3\boldsymbol{r}}{r^5}(\boldsymbol{\mu}\cdot\boldsymbol{r}), \tag{2.3}$$

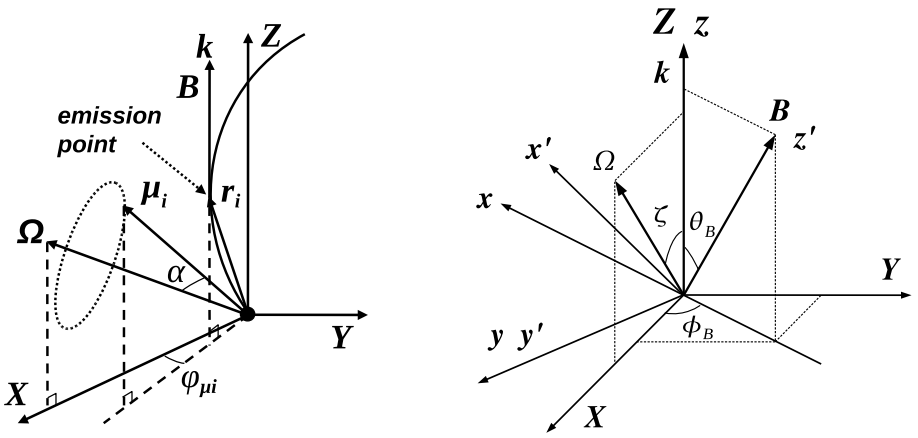

Figure 1. Three frames used in this paper as follows. (1) The fixed frame XYZ with $\hat{\boldsymbol{Z}} \parallel \hat{\boldsymbol{k}}, \boldsymbol{\Omega}$ in the XZ plane and $\hat{\boldsymbol{k}} \times \hat{\boldsymbol{\Omega}} = \Omega \sin\zeta \hat{\boldsymbol{Y}}$. The direction of $\boldsymbol{B}$ in this frame is (θ_B, ϕ_B). (2) The instantaneous inertial frame xyz with $\hat{\boldsymbol{z}} = \hat{\boldsymbol{Z}}$, $\boldsymbol{B}$ in the xz plane and $\hat{\boldsymbol{k}} \times \hat{\boldsymbol{B}} = -\sin\theta_B \hat{\boldsymbol{y}}$. (3) The instantaneous inertial frame $x'y'z'$ with $\hat{\boldsymbol{z}}' = \hat{\boldsymbol{B}}$, $\boldsymbol{k}$ in the $x'z'$ plane and $\hat{\boldsymbol{k}} \times \hat{\boldsymbol{B}} = -\sin\theta_B \hat{\boldsymbol{y}}'$.

with

$$\boldsymbol{\mu}(s) = \mu \left[(\sin\zeta\cos\alpha - \cos\zeta\sin\alpha\cos\Psi)\hat{\boldsymbol{x}} - \sin\alpha\sin\Psi\hat{\boldsymbol{Y}} + (\cos\zeta\cos\alpha + \sin\zeta\sin\alpha\cos\Psi)\hat{\boldsymbol{Z}}\right], \tag{2.4}$$

where α is the inclination angle between $\boldsymbol{\Omega}$ and $\boldsymbol{\mu}$ (see Fig. 1). Note that the impact angle χ, which is the smallest angle between $\boldsymbol{k}$ and $\boldsymbol{\mu}$, is given by $\chi = \zeta - \alpha$. Thus, the polar angles of $\boldsymbol{\mu}$ in the XYZ frame, (θ_μ, ϕ_μ), are given by

$$\cos\theta_\mu = \cos\zeta\cos\alpha + \sin\zeta\sin\alpha\cos\Psi, \qquad \tan\phi_\mu = \frac{-\sin\alpha\sin\Psi}{\sin\zeta\cos\alpha - \cos\zeta\sin\alpha\cos\Psi}. \tag{2.5}$$

The magnetic field at a given point along the ray is inclined at an angle θ_B with respect to the line of sight and make an azimuthal angle ϕ_B in the XY plane such that

$$\cos\theta_B(s) = \frac{B_Z}{B}, \quad \tan\phi_B(s) = \frac{B_Y}{B_X}. \tag{2.6}$$

2.2 Wave evolution equations

The wave equation for photon propagation takes the form

$$\nabla \times (\boldsymbol{\mu}^{-1} \cdot \nabla \times \boldsymbol{E}) = \frac{\omega^2}{c^2}\boldsymbol{\epsilon} \cdot \boldsymbol{E}, \tag{2.7}$$

where $\boldsymbol{E}$ is the electric field and ϵ and $\boldsymbol{\mu}^{-1}$ are the dielectric and inverse permeability tensors, respectively. The inverse permeability is very close to unity when $B \ll B_{\rm Q} = 4.414 \times 10^{13}$ G [the critical quantum electrodynamics (QED) field strength], and we set $\boldsymbol{\mu}$ to be unity in the remainder of this paper. In practice, it is most convenient to calculate the dielectric tensor in the $x'y'z'$ frame (where the z'-axis is along $\boldsymbol{B}$, and $\boldsymbol{k}$ in the $x'z'$ plane; see Fig. 1). Once $[\boldsymbol{\epsilon}]_{x'y'z'}$ (the matrix representation of the dielectric tensor in the $x'y'z'$ frame) is known, we can easily obtain $[\boldsymbol{\epsilon}]_{XYZ}$ in the fixed XYZ frame through a coordinate transformation

$$[\boldsymbol{\epsilon}]_{XYZ} = \boldsymbol{M}[\boldsymbol{\epsilon}]_{x'y'z'}\boldsymbol{M}^{\rm T}, \tag{2.8}$$

where the transformation matrix $\boldsymbol{M}$ is

$$\boldsymbol{M} = \begin{pmatrix} -\cos\phi_B & \sin\phi_B & 0 \\ -\sin\phi_B & -\cos\phi_B & 0 \\ 0 & 0 & 1 \end{pmatrix} \begin{pmatrix} \cos\theta_B & 0 & -\sin\theta_B \\ 0 & 1 & 0 \\ \sin\theta_B & 0 & \cos\theta_B \end{pmatrix} = \begin{pmatrix} -\cos\theta_B\cos\phi_B & \sin\phi_B & \sin\theta_B\cos\phi_B \\ -\cos\theta_B\sin\phi_B & -\cos\phi_B & \sin\theta_B\sin\phi_B \\ \sin\theta_B & 0 & \cos\theta_B \end{pmatrix} \tag{2.9}$$

and $\boldsymbol{M}^{\rm T}$ is the transpose matrix of $\boldsymbol{M}$.

Knowing ϵ along the trajectory, we can use equation (2.7) to derive the wave amplitude evolution equation. Let $\boldsymbol{E} = {\rm e}^{{\rm i}k_0 s}\boldsymbol{A}$, where $k_0 = \omega/c$. Assuming that $|{\rm d}\boldsymbol{A}/{\rm d}s| \ll k_0|\boldsymbol{A}|$ (geometric optics approximation), we obtain

$$\frac{\rm d}{{\rm d}s}\begin{pmatrix} A_X \\ A_Y \end{pmatrix} = \frac{{\rm i}k_0}{2}\begin{bmatrix} \sigma_{XX} & \sigma_{XY} \\ \sigma_{YX} & \sigma_{YY} \end{bmatrix}\begin{pmatrix} A_X \\ A_Y \end{pmatrix}, \tag{2.10}$$

where

$$\sigma_{XX} = \epsilon_{XX} - 1,$$
$$\sigma_{XY} = \epsilon_{XY},$$
$$\sigma_{YX} = \epsilon_{YX},$$
$$\sigma_{YY} = \epsilon_{YY} - 1. \tag{2.11}$$

The wave evolution equation (2.10) can be used to study the evolution of the electromagnetic wave amplitude across the pulsar magnetosphere.

We can also follow the evolution of the four Stokes parameters instead of the evolution of the wave amplitudes. The four Stokes parameters are defined by (in the fixed *XYZ* frame)

$$I = A_X A_X^* + A_Y A_Y^*,$$
$$Q = A_X A_X^* - A_Y A_Y^*,$$
$$U = A_X A_Y^* + A_Y A_X^*,$$
$$V = -\mathrm{i}(A_X A_Y^* - A_Y A_X^*). \tag{2.12}$$

Combining with equation (2.10), we obtain the evolution equations for the Stokes parameters:

$$\frac{\mathrm{d}I}{\mathrm{d}s} = -k_0\frac{\sigma_{XX,\mathrm{i}}+\sigma_{YY,\mathrm{i}}}{2}I - k_0\frac{\sigma_{XX,\mathrm{i}}-\sigma_{YY,\mathrm{i}}}{2}Q - k_0\frac{\sigma_{XY,\mathrm{i}}+\sigma_{YX,\mathrm{i}}}{2}U - k_0\frac{\sigma_{XY,\mathrm{r}}-\sigma_{YX,\mathrm{r}}}{2}V,$$
$$\frac{\mathrm{d}Q}{\mathrm{d}s} = -k_0\frac{\sigma_{XX,\mathrm{i}}-\sigma_{YY,\mathrm{i}}}{2}I - k_0\frac{\sigma_{XX,\mathrm{i}}+\sigma_{YY,\mathrm{i}}}{2}Q - k_0\frac{\sigma_{XY,\mathrm{i}}-\sigma_{YX,\mathrm{i}}}{2}U + k_0\frac{\sigma_{XY,\mathrm{r}}+\sigma_{YX,\mathrm{r}}}{2}V,$$
$$\frac{\mathrm{d}U}{\mathrm{d}s} = -k_0\frac{\sigma_{XY,\mathrm{i}}+\sigma_{YX,\mathrm{i}}}{2}I + k_0\frac{\sigma_{XY,\mathrm{i}}-\sigma_{YX,\mathrm{i}}}{2}Q - k_0\frac{\sigma_{XX,\mathrm{i}}+\sigma_{YY,\mathrm{i}}}{2}U - k_0\frac{\sigma_{XX,\mathrm{r}}-\sigma_{YY,\mathrm{r}}}{2}V,$$
$$\frac{\mathrm{d}V}{\mathrm{d}s} = k_0\frac{\sigma_{XY,\mathrm{r}}-\sigma_{YX,\mathrm{r}}}{2}I - k_0\frac{\sigma_{XY,\mathrm{r}}+\sigma_{YX,\mathrm{r}}}{2}Q + k_0\frac{\sigma_{XX,\mathrm{r}}-\sigma_{YY,\mathrm{r}}}{2}U - k_0\frac{\sigma_{XX,\mathrm{i}}+\sigma_{YY,\mathrm{i}}}{2}V. \tag{2.13}$$

Here, the subscripts 'i' and 'r' correspond to the real and imaginary parts of each element.

If we know the dielectric tensor along the ray, we can integrate equation (2.10) from the emission point in the inner magnetosphere into a large distance where the plasma no longer affects the radiation (both intensity and polarization). We will calculate the dielectric tensor of a relativistic streaming pair plasma in the next section.

3 WAVE MODES AND PROPAGATION IN A STREAMING PLASMA

The magnetospheres of pulsars consist of a relativistic electron–positron pair plasma streaming along magnetic field lines. The Lorentz factor γ of the streaming motion and the plasma density N are uncertain. For the open field line region of radio pulsars, pair cascade simulations generally give $\gamma \sim 10^2$–10^4 and $\eta \equiv N/N_{\rm GJ} \sim 10^2$–$10^5$ (e.g. Daugherty & Harding 1982; Hibschman & Arons 2001; Medin & Lai 2009), while recent theoretical works suggest that the corona of magnetars consists of a pair plasma with γ up to 10^3 and $\eta \sim 2 \times 10^3 (R_*/r)$ (where R_* is the stellar radius; Thompson, Lyutikov & Kulkarni 2002; Beloborodov & Thompson 2007). Here $N_{\rm GJ} = (\Omega B)/(2\pi ec)$ is the Goldreich–Julian density. In this paper, we choose plasma density $\eta = N/N_{\rm GJ}$ to be in the range of 100–1000 and the Lorentz factor γ of the streaming motion to be 100–1000. We also consider a small asymmetry between positrons and electrons, i.e. $\Delta N/N \neq 0$ and $\Delta\gamma/\gamma \neq 0$, where ΔN and $\Delta\gamma$ are the differences in the number densities and Lorentz factors between electrons and positrons, respectively.

3.1 Dielectric tensor

The dielectric tensor ϵ in the $x'y'z'$ frame (with $\hat{\boldsymbol{z}}' = \hat{\boldsymbol{B}}$, $\boldsymbol{k}$ in the $x'z'$ plane and $\hat{\boldsymbol{k}} \times \hat{\boldsymbol{B}} = -\sin\theta_B \hat{\boldsymbol{y}}'$; see Fig. 1) can be written as (see equations 2.11–2.13 and 2.19 of Wang & Lai 2007)

$$[\boldsymbol{\epsilon}]_{x'y'z'} = \begin{bmatrix} \epsilon_{x'x'} & \epsilon_{x'y'} & \epsilon_{x'z'} \\ \epsilon_{y'x'} & \epsilon_{y'y'} & \epsilon_{y'z'} \\ \epsilon_{z'x'} & \epsilon_{z'y'} & \epsilon_{z'z'} \end{bmatrix}, \tag{3.14}$$

where

$$\epsilon_{x'x'} = 1 + \sum_{\rm s} \int f_{\rm s,11} f_{\rm s}(\gamma_{\rm s}) {\rm d}\gamma_{\rm s},$$

$$\epsilon_{x'y'} = -\epsilon_{y'x'} = {\rm i} \sum_{\rm s} \int f_{\rm s,12} f_{\rm s}(\gamma_{\rm s}) {\rm d}\gamma_{\rm s},$$

$$\epsilon_{x'z'} = \epsilon_{z'x'} = -{\rm i} \sum_{\rm s} \int \xi_{\rm s} f_{\rm s,11} f_{\rm s}(\gamma_{\rm s}) {\rm d}\gamma_{\rm s},$$

$$\epsilon_{y'z'} = \epsilon_{z'y'} = \sum_{\rm s} \int \xi_{\rm s} f_{\rm s,12} f_{\rm s}(\gamma_{\rm s}) {\rm d}\gamma_{\rm s},$$

$$\epsilon_{z'z'} = 1 + \sum_{\rm s} \int \left(f_{\rm s,\eta} + \xi_{\rm s}^2 f_{\rm s,11} \right) f_{\rm s}(\gamma_{\rm s}) {\rm d}\gamma_{\rm s}. \tag{3.15}$$

with

$$f_{\rm s,11} = -\frac{v_{\rm s} \gamma_{\rm s}^{-1} (1 + {\rm i}\gamma_{\rm rad})}{(1 + {\rm i}\gamma_{\rm rad})^2 - u_{\rm s} \gamma_{\rm s}^{-2} (1 - n\beta_{\rm s} \cos\theta_B)^{-2}},$$

$$f_{\rm s,12} = -\frac{{\rm sign}\,(q_{\rm s})\, u_{\rm s}^{1/2} v_{\rm s} \gamma_{\rm s}^{-2} (1 - n\beta_{\rm s} \cos\theta_B)^{-1}}{(1 + {\rm i}\gamma_{\rm rad})^2 - u_{\rm s} \gamma_{\rm s}^{-2} (1 - n\beta_{\rm s} \cos\theta_B)^{-2}},$$

$$f_{\rm s,\eta} = -\frac{v_{\rm s}}{(1 + {\rm i}\gamma_{\rm rad}) \gamma_{\rm s}^3 (1 - n\beta_{\rm s} \cos\theta_B)^2},$$

$$\xi_{\rm s} = \frac{n\beta_{\rm s} \sin\theta_B}{1 - n\beta_{\rm s} \cos\theta_B}. \tag{3.16}$$

Here the subscript 's' specifies different species ('e' is for electron and 'p' for positron) and $\beta_{\rm s}$, $\gamma_{\rm s}$ and $f_{\rm s}(\gamma_{\rm s})$ are the velocity (divided by c), Lorentz factor and its distribution function, respectively. The dimensionless parameters $u_{\rm s}$ and $v_{\rm s}$ are

$$u = \frac{\omega_{\rm c}^2}{\omega^2}, \quad u_{\rm s} = u, \tag{3.17}$$

$$v = \frac{\omega_{\rm pl}^2}{\omega^2}, \quad v_{\rm s} = \frac{N_{\rm s}}{N} v. \tag{3.18}$$

Here $N_{\rm s}$ is the number density of particles, $N = N_{\rm p} + N_{\rm e}$, and $\omega_{\rm c}$ and $\omega_{\rm pl}$ are the cyclotron and plasma frequencies, respectively, which are given by

$$\nu_{\rm c} = \frac{\omega_{\rm c}}{2\pi} = \frac{1}{2\pi} \frac{eB}{m_{\rm e} c} = 2.795 \times 10^9\, B_{12}\, {\rm GHz} \tag{3.19}$$

$$\nu_{\rm pl} = \frac{\omega_{\rm pl}}{2\pi} = \frac{1}{2\pi} \sqrt{\frac{4\pi N e^2}{m_{\rm e}}} = 8.960 \times 10^3 N^{1/2}\, {\rm Hz} = 2.370\, \eta^{1/2} B_{12}^{1/2} P_{\rm 1s}^{-1/2}\, {\rm GHz}, \tag{3.20}$$

where the magnetic field $B_{12} = B/(10^{12}\,{\rm G})$, the pulsar spin period $P_{\rm 1s} = P/(1\,{\rm s})$ and the dimensionless density $\eta = N/N_{\rm GJ}$ is measured in units of the Goldreich–Julian density, $N_{\rm GJ} = \Omega B/(2\pi ec) \simeq 7.0 \times 10^{10}\, B_{12} P_{\rm 1s}\, {\rm cm}^{-3}$. The refractive index, $n = ck/\omega$, is generally very close to unity, so we can simply set $n \simeq 1$ in equation (3.16) which does not affect the calculation. The radiative damping

$$\gamma_{\rm rad} = \frac{4e^2 \omega_{\rm c}}{3mc^3} \tag{3.21}$$

is important only near the cyclotron resonance [where $\gamma_{\rm s}\omega\,(1 - n\beta\,\cos\theta_B) \simeq \omega_{\rm c}$] and can be neglected at other places. The function sign $(q_{\rm s})$ is equal to -1 for electrons and 1 for positrons.

In this paper we focus on cold streaming plasmas, which means that both electrons and positrons in the streaming plasma have single $\gamma_{\rm s}$ or $f_{\rm s}(\gamma_{\rm s}) = \delta(\gamma_{\rm s} - \gamma_{\rm s,0})$. Thus, we need not integrate across $\gamma_{\rm s}$ when calculating each element of the dielectric tensor in equation (3.15).

When we consider the region $r \ll r_{\rm cyc}$ (the cyclotron resonance radius), we can take the infinite magnetic field limit, and the damping term can be neglected. In this case, the dielectric tensor becomes very simple (e.g. Arons & Barnard 1986):

$$[\boldsymbol{\epsilon}]_{x'y'z'} = \begin{bmatrix} 1 & 0 & 0 \\ 0 & 1 & 0 \\ 0 & 0 & 1 + f_\eta \end{bmatrix}, \tag{3.22}$$

with $f_\eta = -v\gamma^{-3}\,(1 - \beta\,\cos\theta_B)^{-2}$.

3.2 Wave evolution equation for a single γ plasma

In this subsection we consider the polarization evolution equation for a single γ plasma, i.e. all electrons (positrons) have the same $\gamma_{\rm e}(\gamma_{\rm p})$. We assume that there is a small asymmetry between electrons and positrons in $N_{\rm s}$ or $\gamma_{\rm s}$: $\Delta N/N \ll 1$, where $N = N_{\rm p} + N_{\rm e}$, $\Delta N = N_{\rm p} - N_{\rm e}$

(usually $\Delta N/N$ is the reciprocal of the multiplicity of the cascade), and/or $\Delta\gamma/\gamma \ll 1$ [where $\gamma = (\gamma_{\rm p} + \gamma_{\rm e})/2$, $\Delta\gamma = \gamma_{\rm p} - \gamma_{\rm e}$]. In this case, the final matrix elements in the wave evolution equation (2.10) are

$$\begin{aligned}
\sigma_{XX} &= F_{11}(1 + f_\theta \cos^2\phi_B) + F_\eta \sin^2\theta_B \cos^2\phi_B \simeq F_{11} + F_\eta \sin^2\theta_B \cos^2\phi_B,\\
\sigma_{XY} &= F_{11} f_\theta + F_\eta \sin^2\theta_B \sin\phi_B \cos\phi_B - {\rm i}F_{12} \simeq F_\eta \sin^2\theta_B \sin\phi_B \cos\phi_B - {\rm i}F_{12},\\
\sigma_{YX} &= F_{11} f_\theta + F_\eta \sin^2\theta_B \sin\phi_B \cos\phi_B + {\rm i}F_{12} \simeq F_\eta \sin^2\theta_B \sin\phi_B \cos\phi_B + {\rm i}F_{12},\\
\sigma_{YY} &= F_{11}(1 + f_\theta \sin^2\phi_B) + F_\eta \sin^2\theta_B \sin^2\phi_B \simeq F_{11} + F_\eta \sin^2\theta_B \sin^2\phi_B,
\end{aligned} \tag{3.23}$$

with

$$\begin{aligned}
F_{11} &= \sum_{\rm s} f_{{\rm s},11} \simeq -\frac{v\gamma^{-1}}{1 + 2{\rm i}\gamma_{\rm rad} - u\gamma^{-2}(1 - \beta\cos\theta_B)^{-2}} = F_{11,{\rm r}} + {\rm i}F_{11,{\rm i}},\\
F_{12} &= \sum_{\rm s} f_{{\rm s},12} = -\sum_{\rm s} \frac{{\rm sign}(q_{\rm s}) v_{\rm s}\gamma_{\rm s}^{-} u_{\rm s}^{1/2}\gamma_{\rm s}^{-}(1 - \beta_{\rm s}\cos\theta_B)^{-1}}{1 + 2{\rm i}\gamma_{\rm rad} - u_{\rm s}\gamma_{\rm s}^{-2}(1 - \beta_{\rm s}\cos\theta_B)^{-2}} = F_{12,{\rm r}} + {\rm i}F_{12,{\rm i}},\\
F_\eta &= \sum_{\rm s} f_{{\rm s},\eta} \simeq -v\gamma^{-3}(1 - \beta\cos\theta_B)^{-2},\\
f_\theta &= (\cos\theta_B - \xi\sin\theta_B)^2 - 1 \simeq -\frac{4\theta_B^2\gamma^2}{(1 + \theta_B^2\gamma^2)^2}.
\end{aligned} \tag{3.24}$$

In the derivation of equation (3.23), we have assumed $\theta_B\gamma \gg 1$ (which is valid for most places) so that $f_\theta \simeq 0$.

Using equations (2.13) and (3.23), we can write the evolution equation of the four Stokes parameters as

$$\begin{aligned}
\frac{{\rm d}I}{{\rm d}s} &= -k_0 F_{11,{\rm i}} I - k_0 F_{12,{\rm i}} V,\\
\frac{{\rm d}Q}{{\rm d}s} &= -k_0 F_{11,{\rm i}} Q + k_0 F_{12,{\rm r}} U + \frac{k_0}{2} F_\eta \sin^2\theta_B \sin 2\phi_B V,\\
\frac{{\rm d}U}{{\rm d}s} &= -k_0 F_{12,{\rm r}} Q - k_0 F_{11,{\rm i}} U - \frac{k_0}{2} F_\eta \sin^2\theta_B \cos 2\phi_B V,\\
\frac{{\rm d}V}{{\rm d}s} &= -k_0 F_{12,{\rm i}} I - \frac{k_0}{2} F_\eta \sin^2\theta_B (Q\sin 2\phi_B - U\cos 2\phi_B) - k_0 F_{11,{\rm i}} V.
\end{aligned} \tag{3.25}$$

Here $k_0 = c/\omega$ and the subscripts 'r' and 'i' specify the real and imaginary parts, respectively. Equation (3.25) is useful for understanding the different kinds of propagation effects on the polarization evolution (see Section 4).

3.3 Wave modes

Using the electric displacement $\boldsymbol{D} = \boldsymbol{\epsilon}\cdot\boldsymbol{E}$ in the Maxwell equations, we obtain the equation for plane waves with $\boldsymbol{E} \propto {\rm e}^{{\rm i}(\boldsymbol{k}\cdot\boldsymbol{r} - \omega t)}$:

$$[\epsilon_{ij} + n^2(\hat{k}_i\hat{k}_j - \delta_{ij})]E_j = 0, \tag{3.26}$$

where $n = ck/\omega$ is the refractive index and $\hat{\boldsymbol{k}} = \boldsymbol{k}/k$. In the coordinate system xyz with $\boldsymbol{k}$ along the z-axis and $\boldsymbol{B}$ in the xz plane (see Fig. 1), we project the above equation in the xy plane and obtain

$$\begin{pmatrix} \eta_{xx} - n^2 & \eta_{xy} \\ \eta_{yx} & \eta_{yy} - n^2 \end{pmatrix} \begin{pmatrix} E_x \\ Ey \end{pmatrix} = 0, \tag{3.27}$$

where

$$\begin{aligned}
\eta_{xx} &= \epsilon_{xx} - \epsilon_{xz}\epsilon_{zx}/\epsilon_{zz},\\
\eta_{xy} &= \epsilon_{xy} - \epsilon_{xz}\epsilon_{zy}/\epsilon_{zz},\\
\eta_{yx} &= \epsilon_{yx} - \epsilon_{yz}\epsilon_{zx}/\epsilon_{zz},\\
\eta_{yy} &= \epsilon_{yy} - \epsilon_{yz}\epsilon_{zy}/\epsilon_{zz}.
\end{aligned} \tag{3.28}$$

From equation (3.27), we obtain two eigenmodes, to be labelled as the plus (+) mode and minus (−) mode, respectively. The refractive indices of the two modes are given by

$$n_\pm^2 = \frac{(\eta_{xx} + \eta_{yy}) \pm \sqrt{(\eta_{xx} - \eta_{yy})^2 + 4\eta_{xy}\eta_{yx}}}{2}. \tag{3.29}$$

We write the mode polarization vector as $\boldsymbol{E}_\pm = \boldsymbol{E}_{\pm T} + \boldsymbol{E}_{\pm z}\hat{\boldsymbol{z}}$ in the xyz frame, with the transverse part given by

$$\boldsymbol{E}_{\pm T} = \frac{1}{(1 + K_\pm^2)^{1/2}}(K_\pm, 1), \tag{3.30}$$

where

$$K_\pm = \left(\frac{E_x}{E_y}\right)_\pm = -\frac{\eta_{yy} - n_\pm^2}{\eta_{yx}} = \frac{(\eta_{xx} - \eta_{yy}) \pm \sqrt{(\eta_{xx} - \eta_{yy})^2 + 4\eta_{xy}\eta_{yx}}}{2\eta_{yx}} \tag{3.31}$$

describes the polarization state of the two eigenmodes.

From the dielectric tensor of the relativistic streaming pair plasma given by equations (3.14)–(3.16), we obtain the tensor components in the *xyz* coordinate system:

$$\begin{aligned}
\epsilon_{xx} &= \epsilon_{x'x'}\cos^2\theta_B + \epsilon_{z'z'}\sin^2\theta_B - (\epsilon_{x'z'} + \epsilon_{z'x'})\sin\theta_B\cos\theta_B,\\
\epsilon_{yy} &= \epsilon_{y'y'},\\
\epsilon_{zz} &= \epsilon_{x'x'}\sin^2\theta_B + \epsilon_{z'z'}\cos^2\theta_B + (\epsilon_{x'z'} + \epsilon_{z'x'})\sin\theta_B\cos\theta_B,\\
\epsilon_{xy} &= -\epsilon_{yx} = \epsilon_{x'y'}\cos\theta_B - \epsilon_{z'y'}\sin\theta_B,\\
\epsilon_{xz} &= \epsilon_{zx} = (\epsilon_{x'x'} - \epsilon_{z'z'})\sin\theta_B\cos\theta_B + \epsilon_{x'z'})(\cos^2\theta_B - \sin^2\theta_B),\\
\epsilon_{yz} &= -\epsilon_{zy} = \epsilon_{y'x'}\sin\theta_B + \epsilon_{y'z'}\cos\theta_B.
\end{aligned} \tag{3.32}$$

Combining the above equations with equation (3.27), we find that $\eta_{xy} = -\eta_{yx}$, and η_{yx} is almost purely imaginary (except very close to cyclotron resonance). We define the polarization parameter, $\beta_{\rm pol}$, as

$$\beta_{\rm pol} = -{\rm i}\frac{\eta_{xx} - \eta_{yy}}{2\eta_{yx}} \simeq -{\rm i}\frac{\epsilon_{y'y'} - \epsilon_{x'x'}\cos^2\theta_B - \epsilon_{z'z'}\sin^2\theta_B + (\epsilon_{x'z'} + \epsilon_{z'x'})\sin\theta_B\cos\theta_B}{2(\epsilon_{y'x'}\cos\theta_B - \epsilon_{y'z'}\sin\theta_B)} \tag{3.33}$$

Then equation (3.31) can be written as

$${\rm i}K_\pm = \beta_{\rm pol} \mp {\rm sign}(\eta_{yx,{\rm i}})\sqrt{\beta_{\rm pol}^2 + 1}. \tag{3.34}$$

Here ${\rm sign}(\eta_{yx,{\rm i}})$ means the sign of the imaginary part of η_{yx}. Obviously, when $|\beta_{\rm pol}| \gg 1$, the two eigenmodes are linear polarized, while for $|\beta_{\rm pol}| = 0$ the two modes are circular polarized.

Consider a cold pair plasma with $\Delta N = N_{\rm p} - N_{\rm e} \ll N$ and $\Delta\gamma = \gamma_{\rm p} - \gamma_{\rm e} \ll \gamma$. When the Lorentz-shifted frequency, $\gamma\omega\,(1 - \beta\cos\theta_B)$, is much less than the cyclotron frequency $\omega_{\rm c}$, i.e. for $r \ll r_{\rm cyc}$ or $\lambda = \omega_{\rm c}/[\gamma\omega\,(1 - \beta\cos\theta_B)] = u^{1/2}\gamma^{-1}\,(1 - \beta\cos\theta_B)^{-1} \gg 1$, we have

$$\beta_{\rm pol} \simeq \frac{-\lambda\theta_B^2\gamma^2(1 + \theta_B^2\gamma^2)^{-1}}{(1 - \theta_B^2\gamma^2)\Delta N/N - \Delta\gamma/\gamma}. \tag{3.35}$$

Here we assume $\theta_B \ll 1$ so that $\lambda \simeq 4u^{1/2}\,\gamma(1 + \theta_B^2\gamma^2)^{-1}$. After the photon passes through the cyclotron resonance, $r \gg r_{\rm cyc}$ or $\lambda \ll 1$, the polarization parameter is given by

$$\beta_{\rm pol} \simeq \frac{\lambda\theta_B^2\gamma^2}{\theta_B^2\gamma^2(3 - \theta_B^2\gamma^2)\Delta\gamma/\gamma - (1 - \theta_B^4\gamma^4)\Delta N/N}. \tag{3.36}$$

These expressions are useful for understanding the effect of mode circularization (Section 4.3).

3.4 Evolution of the mode amplitude

In the *xyz* frame [with $\hat{\boldsymbol{z}} = \hat{\boldsymbol{k}}$, $\hat{\boldsymbol{B}} = (-\sin\theta_B, 0, \cos\theta_B)$ in this frame], we know that there are two wave modes: '+' mode and '−' mode. It is convenient to introduce a mixing angle, $\theta_{\rm m}$, via $\tan\theta_{\rm m} = 1/({\rm i}K_+)$, so that

$$\tan 2\theta_{\rm m} = \beta_{\rm pol}^{-1}. \tag{3.37}$$

In the *xyz* frame, the transverse components of the mode eigenvectors are

$$\boldsymbol{E}_+ = \begin{pmatrix} {\rm i}\cos\theta_{\rm m} \\ \sin\theta_{\rm m} \end{pmatrix}, \quad \boldsymbol{E}_- = \begin{pmatrix} -{\rm i}\sin\theta_{\rm m} \\ \cos\theta_{\rm m} \end{pmatrix}, \tag{3.38}$$

In the fixed *XYZ* frame (see Fig. 1), they become

$$\boldsymbol{E}_+ = \begin{pmatrix} {\rm i}\cos\theta_{\rm m}\cos\phi_B - \sin\theta_{\rm m}\sin\phi_B \\ {\rm i}\cos\theta_{\rm m}\sin\phi_B + \sin\theta_{\rm m}\cos\phi_B \end{pmatrix}, \quad \boldsymbol{E}_- = \begin{pmatrix} -{\rm i}\sin\theta_{\rm m}\cos\phi_B - \cos\theta_{\rm m}\sin\phi_B \\ -{\rm i}\sin\theta_{\rm m}\sin\phi_B + \cos\theta_{\rm m}\cos\phi_B \end{pmatrix}. \tag{3.39}$$

The general wave amplitude can be written as

$$\begin{pmatrix} A_X \\ A_Y \end{pmatrix} = A_+\boldsymbol{E}_+ + A_-\boldsymbol{E}_-. \tag{3.40}$$

Substitute this into the wave equation, we obtain the mode amplitude evolution equation:

$${\rm i}\frac{{\rm d}}{{\rm d}s}\begin{pmatrix} A_+ \\ A_- \end{pmatrix} = \begin{bmatrix} -\Delta k/2 + \phi_B'\sin 2\theta_{\rm m} & {\rm i}\theta_{\rm m}' + \phi_B'\cos 2\theta_{\rm m} \\ -{\rm i}\theta_{\rm m}' + \phi_B'\cos 2\theta_{\rm m} & \Delta k/2 - \phi_B'\sin 2\theta_{\rm m} \end{bmatrix}\begin{pmatrix} A_+ \\ A_- \end{pmatrix}, \tag{3.41}$$

where the superscript $(')$ specifies ${\rm d}/{\rm d}\,s$, $\Delta k = k_+ - k_- = \Delta n\omega/c$, and we have subtracted a non-essential unity matrix from the above. This equation generalizes the special cases (where only $\theta_{\rm m}$ or ϕ_B varies) studied in Lai & Ho (2002, 2003) and van Adelsberg & Lai (2006), and it is useful for understanding the effect of mode coupling (Section 4.2).

4 SOME IMPORTANT PROPAGATION EFFECTS

With the equations derived in previous sections, we can now identify several key physical effects relevant for the evolution of wave polarization. We consider the 'weak dispersion' region where the wave frequency is much larger than the plasma frequency in the plasma rest frame and the refractive indices of the two natural wave modes are very close to unity. So we do not discuss the refraction effect here. The detailed discussion about refraction effect can be found in Barnard & Arons (1986).

4.1 Cyclotron resonance/absorption

Cyclotron resonance occurs when the wave frequency in the electron/positron rest frame is close to the cyclotron frequency:

$$\tilde{\omega} = \gamma\omega(1 - \beta\cos\theta_B) = \omega_{\rm c} = \frac{eB}{mc}. \tag{4.42}$$

The eigenmodes at the cyclotron resonance point are always two circular polarized modes (marked as '+' for the left-handed circular polarized mode and '−' for the right-handed one). Since the electrons and positrons have different directions of gyration (one is right-handed and the other one is left-handed), the right-handed circular polarized mode is absorbed by electrons while the left-handed circular polarized mode is absorbed by positrons. For a right-handed circular polarized mode, the scattering cross-section by electrons in the electron rest frame (the physical quantities in the rest frame are marked by '~') is

$$\tilde{\sigma}_- \simeq (2\pi)^2 \frac{e^2}{mc}\delta(\tilde{\omega} - \omega_{\rm c}). \tag{4.43}$$

The optical depth of this mode in the rest frame is

$$\tilde{\tau}_- = \int \tilde{N}_{\rm e}\tilde{\sigma}\,{\rm d}\tilde{s}. \tag{4.44}$$

Since the optical depth is Lorentz invariant, and

$$\tilde{N}_{\rm e} = \gamma^{-1}N_{\rm e}, \quad {\rm d}\tilde{s} = \gamma_{\rm e}(1 - \beta_{\rm e}\cos\theta_B){\rm d}s, \tag{4.45}$$

the optical depth in the 'lab' frame is

$$\tau_- = \tilde{\tau}_- = \int N_{\rm e}\tilde{\sigma}(1 - \beta_{\rm e}\cos\theta_B){\rm d}s. \tag{4.46}$$

For a simple model, we set

$$B(r) \simeq B_*\left(\frac{R_*}{r}\right)^3, \quad N_{\rm e}(r) \simeq \eta_{\rm e}\frac{\Omega B(r)}{2\pi ec} \tag{4.47}$$

with B_* being the surface magnetic field. Thus, the optical depth is given by (e.g. Rafikov & Goldreich 2005)

$$\tau_- \simeq \frac{2\pi}{3}\eta_{\rm e}(1 - \beta_{\rm e}\cos\theta_B)\frac{r_{e,{\rm cyc}}}{c/\Omega} \simeq 0.62\eta B_{*12}^{1/3}\gamma_{\rm e}^{-1/3}\nu_9^{-1/3}P_{\rm 1s}^{-1}(1 - \beta_{\rm e}\cos\theta_B)^{2/3} \tag{4.48}$$

with $B_{*12} = B_*/(10^{12}\,{\rm G})$ and $\nu_9 = \nu/(10^9\,{\rm Hz})$. From equation (4.42), we can find the resonance radius of the electron

$$r_{\rm e,cyc}/R_* = 1.8 \times 10^3 B_{*12}^{1/3}\nu_9^{-1/3}\gamma_{\rm e}^{-1/3}\theta_B^{-2/3}. \tag{4.49}$$

Here θ_B is the $\boldsymbol{k}$–$\boldsymbol{B}$ angle at the resonance radius.

The optical depth of the left-handed circular polarized mode caused by the scattering of positrons is similarly given by

$$\tau_+ \simeq \frac{2\pi}{3}\eta_{\rm p}(1 - \beta_{\rm p}\cos\theta_B)\frac{r_{\rm p,cyc}}{c/\Omega} \tag{4.50}$$

with $\eta_{\rm p} = N_{\rm p}/N_{\rm GJ}$, and $r_{\rm p,cyc}$ is defined by equation (4.49) using $\gamma_{\rm p}$ instead of $\gamma_{\rm e}$.

When there is an asymmetry between electrons and positrons (different density and/or different γ), the optical depths of the two modes are different:

$$\Delta\tau = \tau_+ - \tau_- = 2\tau\left(\frac{\Delta N}{N} - \frac{\Delta\gamma}{6\gamma}\right), \tag{4.51}$$

with $\tau \simeq \tau_+ \simeq \tau_-$. Now consider a linear-polarized photon propagating through the cyclotron resonance region. The mode evolution is non-adiabatic (which is always the case since the resonance happens after the polarization limiting radius; see Section 4.2). Before the resonance, the total intensity is

$$I_{\rm i} = I_{\rm i,+} + I_{\rm i,-}, \quad \text{with} \quad I_{\rm i,+} = I_{\rm i,-}, \tag{4.52}$$

which means that the intensities of the two circular-polarized modes are the same. The wave intensity after the cyclotron absorption is

$$I_{\rm f} = I_{\rm f,+} + I_{\rm f,-} = I_{\rm i,+}{\rm e}^{-\tau_+} + I_{\rm i,-}{\rm e}^{-\tau_-}. \tag{4.53}$$

Because of the difference between τ_+ and τ_-, the final intensities of the two circular-polarized modes are different. Thus, CP can be generated:

$$V_{\rm f} = I_{\rm f,+} - I_{\rm f,-} = I_{\rm i,+}{\rm e}^{-\tau_+} - I_{\rm i,-}{\rm e}^{-\tau_-}. \tag{4.54}$$

$$\frac{V_{\rm f}}{I_{\rm f}} = \frac{{\rm e}^{-\tau_+} - {\rm e}^{-\tau_-}}{{\rm e}^{-\tau_+} + {\rm e}^{-\tau_-}}. \tag{4.55}$$

When $\tau_\pm \ll 1$, $V_{\rm f}/I_{\rm f} = -\Delta\tau/2 = \tau\left(\frac{\Delta\gamma}{6\gamma} - \frac{\Delta N}{N}\right)$.

We can also obtain the same result formally by using the Stokes parameters' evolution equation (3.25). Since electrons and positrons have slightly different γ, the cyclotron absorptions caused by electrons and positrons occur at different radii. We analyse them separately. Consider the cyclotron absorption caused by electrons first. Near the resonance, with

$$x = \frac{r - r_{\rm e,cyc}}{r_{\rm e,cyc}}, \quad |x| \ll 1, \tag{4.56}$$

we have

$$u\gamma_{\rm e}^{-2}(1 - \beta\cos\theta_B)^{-2} \simeq \left(\frac{r}{r_{\rm e,cyc}}\right)^{-6} = (1-x)^6 \simeq 1 - 6x, \tag{4.57}$$

where we have assumed $B \propto r^{-3}$. The imaginary parts of F_{11} and F_{12} in equation (3.25) are

$$F_{11,{\rm i}} = f_{{\rm e},11,{\rm i}} = {\rm Im}(f_{{\rm e},11}) \simeq {\rm Im}\left(-\frac{v_{\rm e}\gamma^{-1}}{2{\rm i}\gamma_{\rm rad} + 6x}\right) = \frac{v_{\rm e}\gamma^{-1}}{2\gamma_{\rm rad}}\frac{1}{1 + (3x/\gamma_{\rm rad})^2}, \tag{4.58}$$

$$F_{12,{\rm i}} = f_{{\rm e},12,{\rm i}} = {\rm Im}(f_{{\rm e},12}) \simeq {\rm Im}\left[-f_{{\rm e},11}(1+x)^3\right] \simeq -f_{{\rm e},11,{\rm i}}. \tag{4.59}$$

Also $|F_\eta| \ll |f_{{\rm e},11,{\rm i}}|$ near the resonance, so we neglect it. Thus, the evolution equation for I and V in equation (3.25) are simplified to

$$\begin{aligned} {\rm d}I/{\rm d}r &= -k_0 f_{{\rm e},11,{\rm i}} I + k_0 f_{{\rm e},11,{\rm i}} V, \\ {\rm d}V/{\rm d}r &= k_0 f_{{\rm e},11,{\rm i}} I - k_0 f_{{\rm e},11,{\rm i}} V. \end{aligned} \tag{4.60}$$

Then we have

$$\begin{aligned} {\rm d}I_+/{\rm d}r &= 0, \\ {\rm d}I_-/{\rm d}r &= -2k_0 f_{{\rm e},11,{\rm i}} I_-, \end{aligned} \tag{4.61}$$

with $I_+ = (I + V)/2$ being the intensity of the left circular-polarized mode and $I_- = (I - V)/2$ of the right one. The solution to these equations is

$$\begin{aligned} I_{\rm f} &= I_{{\rm i},+} + I_{{\rm i},-}{\rm e}^{-\tau_-} \\ V_{\rm f} &= I_{{\rm i},+} + I_{{\rm i},-}{\rm e}^{-\tau_-}, \end{aligned} \tag{4.62}$$

where $I_{{\rm i},+}$, $I_{{\rm i},-}$ are the circular-polarized mode intensities before the resonance, and

$$\tau_- = \int_{\rm acrossCR} 2k_0 f_{{\rm e},11,{\rm i}}{\rm d}r = \frac{2\pi}{3}\eta_{\rm e}(1 - \beta_{\rm e}\cos\theta_B)\frac{r_{\rm e,cyc}}{c/\Omega}, \tag{4.63}$$

in agreement with equation (4.48). For the cyclotron absorption by positrons, the analysis is exactly the same, except $f_{{\rm p},12} = f_{{\rm p},11}(1+x)^3 \simeq f_{{\rm p},11}$. The intensities' evolution equations are

$$\begin{aligned} {\rm d}I_+/{\rm d}r &= -2k_0 f_{{\rm p},11,{\rm i}} I_+, \\ {\rm d}I_-/{\rm d}r &= 0. \end{aligned} \tag{4.64}$$

Including both cyclotron absorption by electrons and positrons, the intensity and Stokes V parameters after the resonance are

$$\begin{aligned} I_{\rm f} &= I_{{\rm i},+}{\rm e}^{-\tau_+} + I_{{\rm i},-}{\rm e}^{-\tau_-} \\ V_{\rm f} &= I_{{\rm i},+}{\rm e}^{-\tau_+} - I_{{\rm i},-}{\rm e}^{-\tau_-} \end{aligned} \tag{4.65}$$

with

$$\tau_+ = \int_{\rm acrossCR} 2k_0 f_{{\rm p},11,{\rm i}}{\rm d}r = \frac{2\pi}{3}\eta_{\rm p}(1 - \beta_{\rm p}\cos\theta_B)\frac{r_{\rm p,cyc}}{r_{\rm lc}}. \tag{4.66}$$

Thus, our evolution equations for the mode and Stokes parameters derived in Section 3 automatically include the correct physics of cyclotron absorption by electrons and positrons.

4.2 Wave mode coupling

Wave mode coupling happens near the 'polarization limiting radius', $r_{\rm pl}$, where the mode evolution changes from adiabatic to non-adiabatic, i.e. from $\Gamma_{\rm ad}(r < r_{\rm pl}) > 1$ to $\Gamma_{\rm ad}(r > r_{\rm pl}) < 1$.[1] Generally, this is caused by the rotation of the pulsar. Obviously, the concept of wave mode

[1] Some previous papers (e.g. Barnard 1986) define the 'polarization limiting radius' $r_{\rm pl}$ as the cyclotron resonance radius since near $r_{\rm cyc}$, the adiabaticity parameter becomes larger than unity and then immediately drops below unity (see e.g. Fig. 4). However, note that for a quasi-symmetric pair plasma (which means that the electrons and positrons have almost same number densities and velocities) of interest in our paper, the cyclotron absorption almost does not affect the polarization state (Q/I, U/I, V/I). Also, even for an asymmetric plasma, the cyclotron resonance occurs over a rather small distance, and its effect can be treated accurately using the equations described in Section 4.1. Therefore, we will just define the $r_{\rm pl}$ as the boundary of adiabatic mode evolution away from the cyclotron resonance (i.e. regardless where the cyclotron absorption occurs).

coupling is relevant for determining the observed polarization only when the wave mode is linear polarized, i.e. $r_{\rm pl} < r_{\rm cir}$ (see Section 4.3). In the process of wave mode coupling, the CP will be generated. For $r < r_{\rm cir}$ (so that $\theta_{\rm m} = 0$ or $\pi/2$), the mode amplitude evolution equation (3.41) simplifies to

$$\mathrm{i}\frac{\mathrm{d}}{\mathrm{d}s}\begin{pmatrix} A_+ \\ A_- \end{pmatrix} = \begin{pmatrix} -\Delta k/2 & \mathrm{i}\phi'_B \\ -\mathrm{i}\phi'_B & \Delta k/2 \end{pmatrix}\begin{pmatrix} A_+ \\ A_- \end{pmatrix}, \tag{4.67}$$

with $\Delta k = \Delta n\omega/c$. The adiabatic parameter is defined as

$$\Gamma_{\rm ad} = \left|\frac{\Delta n\omega}{2c\phi'_B}\right|, \tag{4.68}$$

where

$$\Delta n = \frac{1}{2}\{f_\eta \sin\theta_B^2 - f_{11}[1-(\cos\theta_B - \xi\sin\theta_B)^2]\}. \tag{4.69}$$

When $r < r_{\rm cyc}$, $\Delta n \simeq 1/2 f_\eta \sin^2\theta_B \simeq -2v\theta_B^{-2}\gamma^{-3}$, so we have

$$\Gamma_{\rm ad} = 5.6\times10^9 \eta B_{12}\nu_9^{-1}\theta_B^{-2}\gamma^{-3}|F_\phi|^{-1}, \tag{4.70}$$

where we have used $\phi'_B = F_\phi/r_{\rm lc}$, $r_{\rm lc} = c/\Omega$, and

$$F_\phi = \frac{\sin^2\alpha\cos\zeta - \sin\alpha\cos\alpha\sin\zeta\cos\psi}{1-(\cos\alpha\cos\zeta+\sin\zeta\sin\alpha\cos\psi)^2}. \tag{4.71}$$

Obviously, $\Gamma_{\rm ad} \gg 1$ means adiabatic mode evolution while $\Gamma_{\rm ad} \ll 1$ means non-adiabatic. The condition $\Gamma_{\rm ad}(r = r_{\rm pl}) = 1$ then gives the polarization limiting radius

$$r_{\rm pl}/R = 1.8\times10^3\eta^{1/3}B_{*12}^{1/3}\nu_9^{-1/3}\theta_B^{-2/3}\gamma^{-1}|F_\phi|^{-1/3}. \tag{4.72}$$

Here θ_B is the $\boldsymbol{k}$–$\boldsymbol{B}$ angle at $r = r_{\rm pl}$. Comparing $r_{\rm pl}$ with $r_{\rm cyc}$ (see equation 4.49), we have

$$r_{\rm pl}/r_{\rm cyc} = \eta^{1/3}\gamma^{-2/3}\left(\frac{\theta_{B,\rm pl}}{\theta_{B,\rm cyc}}\right)^{-2/3}|F_\phi|^{-1/3} = 0.215\eta_2^{1/3}\gamma_2^{-2/3}\left(\frac{\theta_{B,\rm pl}}{\theta_{B,\rm cyc}}\right)^{-2/3}|F_\phi|^{-1/3} \lesssim 1. \tag{4.73}$$

So in the typical parameter region ($\eta = 100$, $\gamma = 100$, $|F_\phi|=$ a few), wave mode coupling always occurs before cyclotron absorption.

To understand the wave mode coupling around $r_{\rm pl}$, we write

$$\Gamma_{\rm ad} = x^{-n}, \tag{4.74}$$

with $x = r/r_{\rm pl}$. According to equation (4.70), the power-law index $n \sim 3$ (not exactly 3 because θ_B also varies as r changes). Then equation (4.67) can be simplified to

$$\mathrm{i}\frac{\mathrm{d}}{\mathrm{d}x}\begin{pmatrix} A_+ \\ A_- \end{pmatrix} = |\Lambda|\begin{pmatrix} x^{-n} & \mathrm{sign}(\phi'_B)\mathrm{i} \\ -\mathrm{sign}(\phi'_B)\mathrm{i} & -x^{-n} \end{pmatrix}\begin{pmatrix} A_+ \\ A_- \end{pmatrix}, \tag{4.75}$$

where

$$\Lambda \equiv r_{\rm pl}\phi'_B = 0.38\mathrm{sign}(\phi'_B)\eta^{1/3}B_{*12}^{1/3}\nu_9^{-1/3}\theta_B^{-2/3}\gamma^{-1}P_1^{-1}|F_\phi|^{2/3}. \tag{4.76}$$

A similar equation is given by van Adelsberg & Lai (2006), except that in their paper the dispersion relation of X-ray is dominated by QED effect so that $\Delta n > 0$, while in our case plasma effect dominates the radio wave propagation with $\Delta n < 0$. Fig. 2 shows two examples of mode evolution with $\Lambda = 0.1$ and $\Lambda = 1.0$, both for $n = 3$. The photon is 100 per cent linear polarized before the wave mode coupling (here we set it to be O mode initially). After the wave mode coupling ($x \gg 1$), the polarization states are frozen. In this process, CP is produced. It is obvious that the larger the Λ is, the more CP will be generated. Fig. 3 shows how the value of Λ affects the final CP $|V|/I$ when the power index $n = 3$. For $n = 3$ and $\Lambda < 0.1$, the final CP is given by the expression

$$V/I = 2.2\mathrm{sign}(\phi'_B)|\Lambda|^{3/2}. \tag{4.77}$$

For $\Lambda \gtrsim 1$, the CP $|V|/I$ is close to 1. Equation (4.77) also shows the relationship between the sign of the CP and ϕ'_B. An increasing ϕ_B (or $\phi'_B > 0$) corresponds to positive CP while decreasing ϕ_B to the negative one.

4.3 Circularization

Circularization happens when $|\beta_{\rm pol}| \sim 1$, and we can define the radius of circularization $r_{\rm cir}$ by $|\beta_{\rm pol}(r = r_{\rm cir})| = 1$. For $r \gg r_{\rm cir}$, the normal modes become circular polarized.

According to equation (3.35), if $r_{\rm cir} \ll r_{\rm cyc}$ (or $\lambda \gg 1$, before cyclotron resonance) and $\theta_B\gamma \gg 1$, the polarization parameter

$$|\beta_{\rm pol}| \simeq \frac{\lambda}{\theta_B^2\gamma^2\Delta N/N - \Delta\gamma/\gamma} \gg 1, \tag{4.78}$$

which means that the two wave modes are always linear polarized. However, if $r_{\rm cir} \ll r_{\rm cyc}$ and $\theta_B\gamma \ll 1$,

$$|\beta_{\rm pol}| \simeq \frac{\lambda\theta_B^2\gamma^2}{\Delta N/N - \Delta\gamma/\gamma}, \tag{4.79}$$

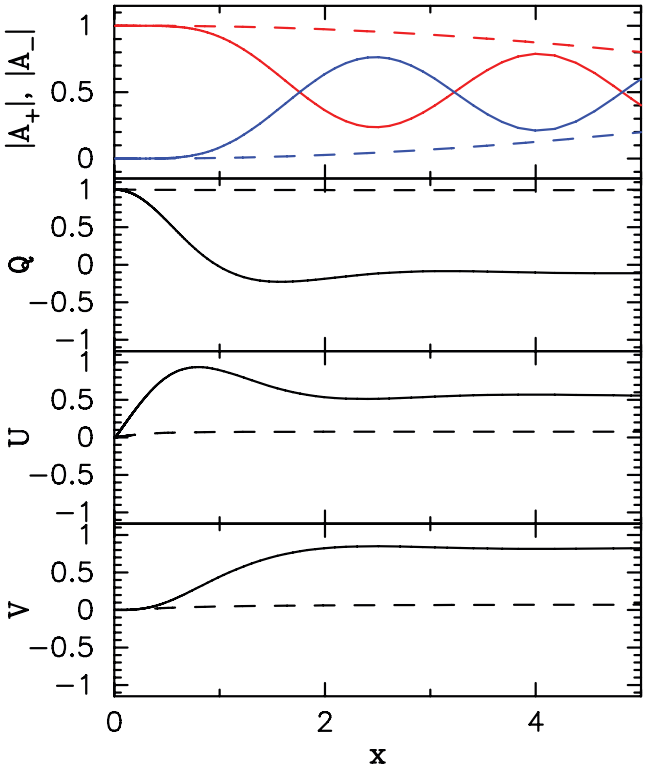

Figure 2. Evolution of the radiation mode amplitudes (top panel) and Stokes parameters (bottom three panels) with power-law index $n = 3$ (see equation 4.74). The solid lines are for $\Lambda = 1.0$ and the dashed lines for $\Lambda = 0.1$. The polarization limiting radius is at $x = 1$. The initial values (at a small $x = x_{\rm i}$) are $A_+ = 1$, $A_- = 0$, $Q = I = 1$, $U = 0$ and $V = 0$. When $x \lesssim 0.5$, the modes evolve adiabatically. At $r \sim r_{\rm pl}$ (or $x = 1$) the modes begin to couple, generating CP. At $x \gg 1$, the Stokes parameters are 'frozen'.

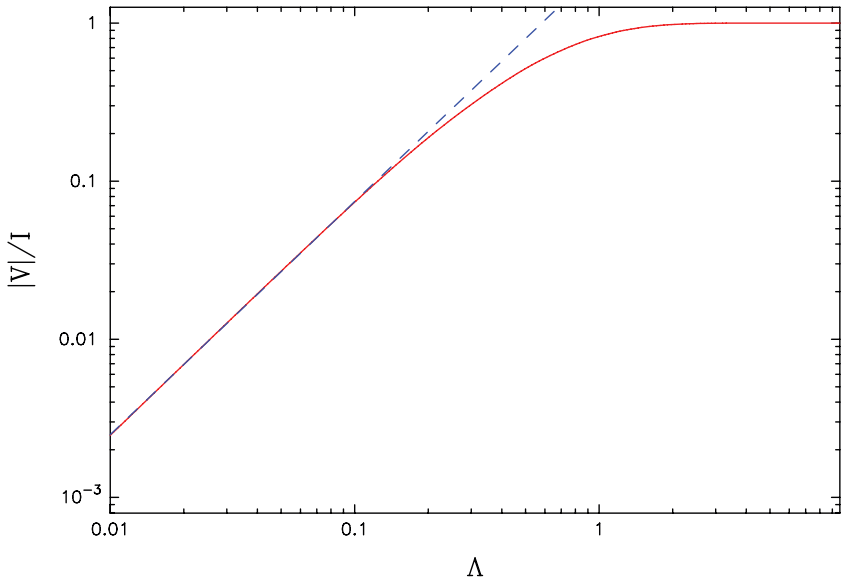

Figure 3. The final CP fraction $|V|/I$ after wave mode coupling as a function of Λ with the power-law index $n = 3$. The LP fraction before wave mode coupling is assumed to be 100 per cent. The dashed line depicts the fitting formula (equation 4.77) for $\Lambda < 0.1$.

so circularization could happen when

$$\theta_B \gamma = \sqrt{(\Delta N/N - \Delta\gamma/\gamma)/\lambda}, \tag{4.80}$$

which implies a very small θ_B. This condition could be satisfied when the photon ray is nearly aligned with the magnetic field or when the photon is generated inside the $1/\gamma$ cone of the radiation beam.

If the circularization happens after the cyclotron resonance ($r_{\rm cir} \gg r_{\rm cyc}$ or $\lambda \ll 1$), according to equation (3.36), the radius of circularization is given by

$$r_{\rm cir}/R_* = 2.2\times 10^3 B_{*12}^{1/3}\nu_9^{-1/3}\theta_B^{-4/3}\gamma^{-1/3}(\Delta N/N - \Delta\gamma/\gamma)^{-1/3}. \quad (4.81)$$

Here we used $B \simeq B_*(r/R_*)^{-3}$ and assumed $\theta_B\gamma \gg 1$. The ratio of $r_{\rm cir}$ to the cyclotron resonance radius (see equation 4.49)) is

$$r_{\rm cir}/r_{\rm cyc} = 1.2\left(\frac{\theta_{B,\rm cir}^2}{\theta_{B,\rm cyc}}\right)^{-2/3}(\Delta N/N - \Delta\gamma/\gamma)^{-1/3} \gg 1. \quad (4.82)$$

Obviously, in the parameter regions we interested in, the circularization radius is typically larger than the cyclotron resonance radius and the polarization limiting radius. Thus, this effect does not change the photon polarization state at all.

4.4 Quasi-tangential propagation effect

In their study of the X-ray polarization signals from magnetized NSs, Wang & Lai (2009) found that as the X-ray photon travels through the magnetosphere, it may cross the region where its wave vector is aligned or nearly aligned with the magnetic field (i.e. θ_B is zero or small). In such a QT region, the azimuthal angle of the magnetic field ϕ_B changes quickly, the two photon modes ($\parallel$ and $\perp$ modes) become (nearly) identical and mode coupling may occur, thereby affecting the polarization alignment. This QT effect generally happens at a few R_* for surface X-ray emission. The physical mechanism is similar to the wave mode coupling effect discussed in Section 4.2 (see the mode evolution equation 2.11 in Wang & Lai 2009), except that the magnetic field plays an important role.

In the radio case, we assume that the photon is emitted in the tangential direction of the magnetic field line at the emission point ($\sim 50R_*$). If the NS is non-rotating, then the $\boldsymbol{k}$–$\boldsymbol{B}$ angle $\theta_B (= 0$ at the emission point) will increase monotonically and no QT effect will occur. However, when we consider the rotation of the NS, for some special photons (e.g. those with a small impact angle χ and special $\Psi_{\rm i}$) θ_B could attain its minimum value at a large radius. As an example, the bottom two panels of Figs 6 and 7 (to be discussed in detail in Section 5) show the evolution of θ_B and ϕ_B along the ray for $\chi = 0.^\circ 5$. We see that θ_B reaches its minimum value at about $s = 700R_*$ away from the emission point. The azimuthal angle ϕ_B changes very quickly at this radius. The two linear modes strongly couple with each other. The final polarization state after crossing this QT region is complicated: $\phi_{\rm PA}$ can be modified significantly and a different sign of CP can be generated for different geometry, which is different from the wave mode coupling effect discussed in Section 4.2. In general, the QT effect strongly influences the polarization phase profiles when the impact angle is very small (see Section 5.3). In our case, the QT effect is always coupled with the wave mode coupling effect (occurring at almost the same place), and the numerical ray integration is necessary to account for these effects accurately (see Section 5).

5 NUMERICAL RESULTS

In Section 4, we have discussed various key physical effects related to wave propagation through the magnetosphere. However, in many cases these different effects are coupled and not easy to separate. Thus, to produced the observed polarization profiles, it is necessary to use the numerical ray integrations to calculate the final wave polarization states.

5.1 Single ray evolution

It is generally accepted that pulsar radio emission is emitted from the open field line region at a few to tens of NS radii (e.g. Cordes 1978; Blaskiewicz et al. 1991; Kramer et al. 1997; Kijak & Gil 2003). In this paper, we choose the emission height $r_{\rm em} = 50R_*$ and assume that at the emission point, the photon is polarized in the $\boldsymbol{k}$–$\boldsymbol{B}$ plane (or the O mode, as in the case of curvature radiation) and propagates along the tangential direction of the local magnetic field line (here we do not consider the emission cone of angle $1/\gamma$). For a given emission height $r_{\rm em}$, the pulsar rotation phase $\Psi_{\rm i}$, the direction of line of sight ζ (which is the $\boldsymbol{k}$–$\boldsymbol{\Omega}$ angle), the surface magnetic field B_* and the plasma properties (plasma density parameter η, Lorentz factor of the streaming plasma γ), we can calculate the dielectric tensor at each point along the photon ray and integrate the wave evolution equation (2.10) from the emission point to a large radius (generally, we choose $r_{\rm lc}/2$), beyond the polarization limiting radius $r_{\rm pl}$ and cyclotron resonance radius $r_{\rm cyc}$, to determine the final polarization state of the photon.

5.1.1 Symmetric pair plasma

We first consider the case of symmetric pair plasmas, i.e. the electrons and positrons have the same Lorentz factors ($\gamma_{\rm p} = \gamma_{\rm e}$ or $\Delta\gamma/\gamma = 0$) and densities ($\Delta N/N = 0$). In this case, the eigenmodes are always linear polarized (mixing angle $\theta_{\rm m} = 0^\circ$ or 90°). Fig. 4 shows an example of the photon polarization evolution along its trajectory. We can clearly find that the wave mode coupling effect (at $r_{\rm pl} \sim 800\,R_*$) occurs before the cyclotron absorption effect (at $r_{\rm cyc} \sim 1700R_*$). According to equation (4.73), for typical plasma parameters: $\eta = 100$, $\gamma = 100$, the polarization limiting radius is always smaller than the cyclotron resonance radius. The final polarization PA, $\phi_{\rm PA}$, is determined by $\phi_B(r_{\rm pl})$ (see equation 5.87). It is obvious that near the polarization limiting radius, $\Gamma_{\rm ad} \propto (r/r_{\rm pl})^{-n}$ and $n \sim 3$, so that as discussed in Section 4.2, the final CP is determined by the value of Λ (see equation 4.77). Since we are dealing with a symmetric pair plasma here, cyclotron absorptions do not change the polarization state (but decrease the total intensity).

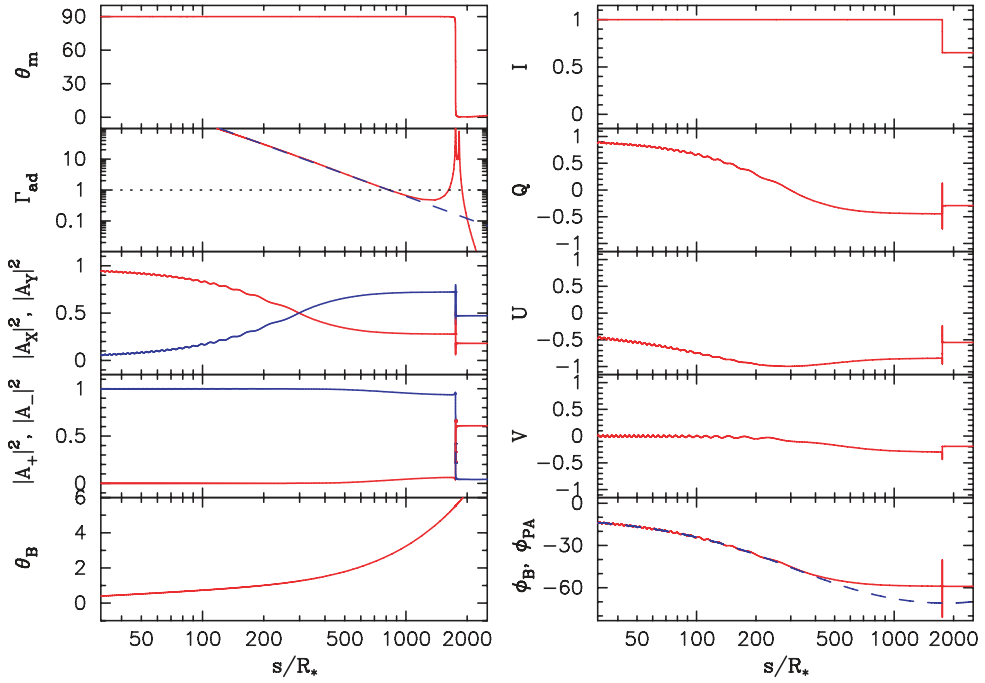

Figure 4. A typical single photon evolution across the magnetosphere. The horizontal axis s/R_* is the photon distance away from the emission point. On the left-hand panels, $\theta_{\rm m}$ is the mode mixing angle defined by equation (3.37), $\Gamma_{\rm ad}$ is the adiabatic parameter defined by equation (4.70) (the dashed line is the power-law fit of $\Gamma_{\rm ad}$ around $r_{\rm pl}$, which is $\Gamma_{\rm ad} \propto s^{-2.39}$), and A_X and A_Y are the wave amplitudes in the fixed XYZ frame. A_+ and A_- are the mode amplitudes and θ_B is the angle between $\boldsymbol{k}$ and $\boldsymbol{B}$. On the right-hand panels, I, Q, U, V are the Stokes parameters, $\phi_{\rm PA} = 0.5\tan^{-1}(U/Q)$ is the LP PA (solid line) and ϕ_B is the azimuthal angle of the $\boldsymbol{B}$ field (dashed line). The initial polarization is assumed to be in the ordinary mode, with $A_+ = 1$, $A_- = 0$. For this example, the parameters are the surface magnetic field $B_* = 10^{12}$ G, NS spin period $P = 1$ s, wave frequency $\nu = 1$ GHz, plasma density parameter $\eta = N/N_{\rm GJ} = 400$ ($N = N_{\rm e} + N_{\rm p}$ and $N_{\rm e} = N_{\rm p}$), Lorentz factor $\gamma = 100$ (with $\Delta\gamma/\gamma \simeq 0$), inclination angle $\alpha = 30^\circ$, impact angle $\chi = 2^\circ$, initial rotation phase $\Psi_{\rm i} = 0^\circ$ and emission height $r_{\rm em} = 50R_*$.

Fig. 5 gives some other examples of the evolution of Stokes parameters with different plasma density η and Lorentz factor γ. Different η and γ correspond to different $r_{\rm pl}$ (according to equation 4.72, lower η and higher γ correspond to a smaller $r_{\rm pl}$) so that the final $\phi_{\rm PA}$ is different too. In all the above cases, the final polarization state changes significantly not only the linear PA but also the CP as compared to the original state.

At the special parameter region of the initial rotation phase $\Psi_{\rm i}$, the QT effect (see Section 4.4) can strongly affect the final polarization state. Fig. 6 shows the photon evolution for $\Psi_{\rm i} = -9^\circ$ (the other parameters are the same as in Fig. 4, e.g. the impact angle $\chi = 2^\circ$). Note that in contrast to Fig. 4, here the $\boldsymbol{k}$–$\boldsymbol{B}$ angle θ_B does not vary monotonically along the ray. There exists a QT region around $s \sim 700R_*$, where θ_B is the minimum and ϕ_B is changing very quickly. As discussed in Section 4.4, the final $\phi_{\rm PA}$ and CP are different from the prediction of pure wave mode coupling effect (which is the case in Fig. 4 where the QT effect does not occur). For the photon evolution with a smaller photon impact angle $\chi = 0.^\circ 5$ (but the initial rotation phase and other parameters are the same as in Fig. 6), the QT effect is stronger, as shown in Fig. 7. Note that even the sign of the final CP in this figure is positive, as a result of the strong QT effect.

5.1.2 Asymmetric pair plasma

If the electrons and positrons of the magnetospheric plasma have different velocities and/or densities, the wave eigenmodes cannot always be linearly polarized. As discussed in Section 4.3, before cyclotron resonance the natural modes are linearly polarized (see equation 4.78) for $\theta_B\gamma \gg 1$. After the cyclotron resonance, the natural modes become elliptical polarized. In Section 4.3, we have defined a circularization radius $r_{\rm cir}$ where the polarization parameter $|\beta_{\rm pol}| = 1$ (see equations 4.81 and 4.82). For $r \gg r_{\rm cir}$, the natural modes become circular polarized.

According to equation (4.73), for typical plasma parameters of interest in this paper, $\eta \gtrsim 100$ and $\gamma \gtrsim 100$, wave mode coupling always occurs before the cyclotron resonance ($r_{\rm pl} < r_{\rm cyc}$). Thus, circularization always happens after wave mode coupling, at which point the wave polarization state is already frozen. Therefore, the change of the natural mode does not affect the observed polarization state. Fig. 8 shows the photon evolution in an asymmetric pair plasma. Note that the mode mixing angle $\theta_{\rm m}$ changes from $0^\circ/90^\circ$ to 45° after the cyclotron resonance, but the polarization state does not change since $r_{\rm cir} > r_{\rm pl}$.

von Hoensbroech et al. (1998) studied wave modes in a pure electron plasma. They assumed that the background plasma has a much lower Lorentz factor (e.g. $\gamma_{\rm bg} = 1.7$) than the Lorentz factor of the radiating beam. In this case, $r_{\rm cir}$ may be close to $r_{\rm pl}$ and CP may be generated around $r_{\rm cir}$. Note that they did not calculate $r_{\rm pl}$ but simply assumed that the final photon polarization is determined by the normal mode at some fixed $r_{\rm pl}$.

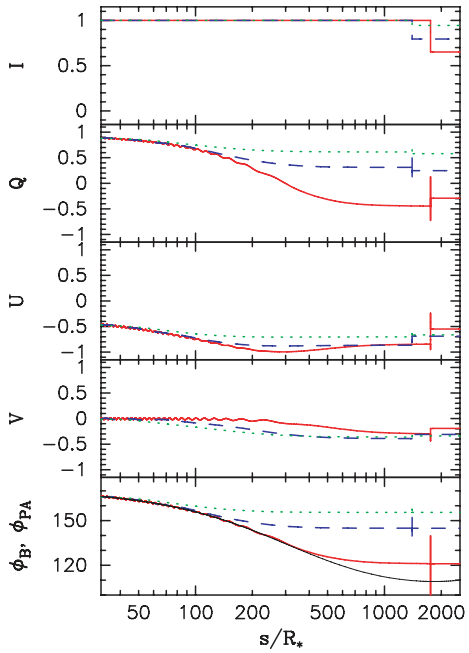

Figure 5. Same as the right-hand panels of Fig. 4, except for different plasma density η and Lorentz factor of the streaming motion γ: the solid lines are for $\eta = 400$, $\gamma = 100$ (same as Fig. 4); the dashed lines for $\eta = 400$, $\gamma = 300$ and the dotted lines for $\eta = 100$, $\gamma = 100$. The thin line in the bottom panel is for ϕ_B. It is obvious that for lower density and/or higher γ, the wave mode coupling occurs at smaller $r_{\rm pl}$.

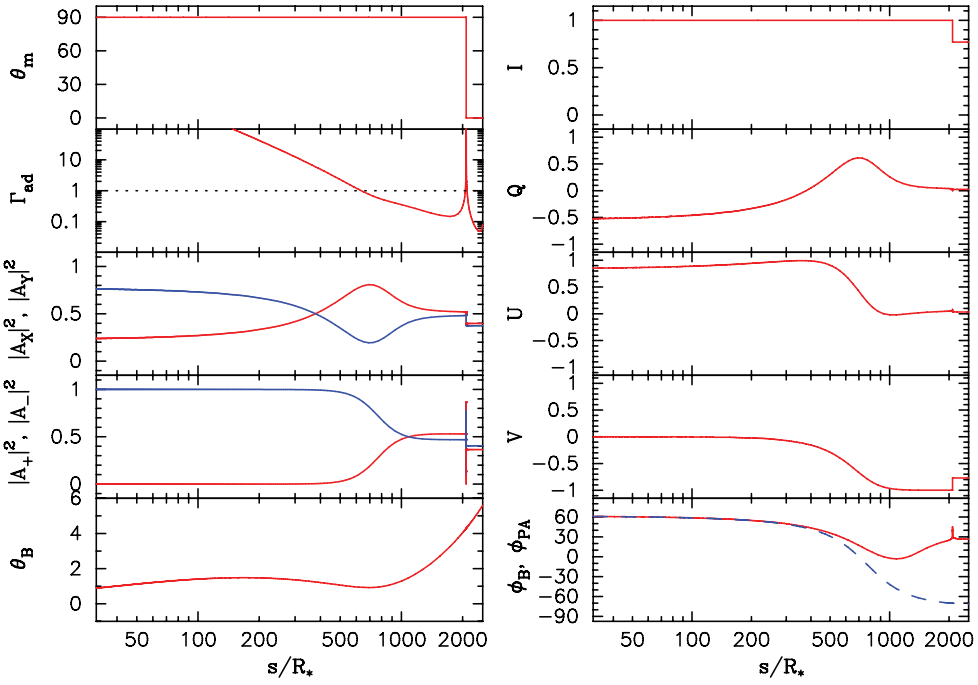

Figure 6. Same as Fig. 4, except for a different initial rotation phase $\Psi_{\rm i} = -9°$. The impact angle is the same as in Fig. 4, $\chi = 2°$. Note that in contrast to Fig. 4, here the $\boldsymbol{k}$–$\boldsymbol{B}$ angle θ_B does not vary monotonically along the ray. There exists a QT region around $s \sim 700R_*$, where θ_B is the minimum and ϕ_B changes very quickly. Strong CP is generated here and the final PA angle $\phi_{\rm PA}$ cannot be predicted by simply using equation (5.84).

5.2 Polarization profiles of the pulsar emission beam

Having understood the main features of polarization evolution along a single ray, we now proceed to calculate the polarization profiles of the pulsar emission beam. To do this, one needs to know the emission height as a function of the pulsar rotation phase. For simplicity, in this paper, we assume that all emissions are from the same height, at $r_{\rm em} = 50R_*$, and defer the results for emissions from a range of heights to a future paper. For a given emission height $r_{\rm em}$, the pulsar rotation phase $\Psi_{\rm i}$, the inclination angle α and the direction of line of sight ζ (which is the $\boldsymbol{k}$–$\boldsymbol{\Omega}$ angle), we can find the position of the emission point $\boldsymbol{r}_{\rm i}$ where the tangential magnetic field line direction is along the line of sight.

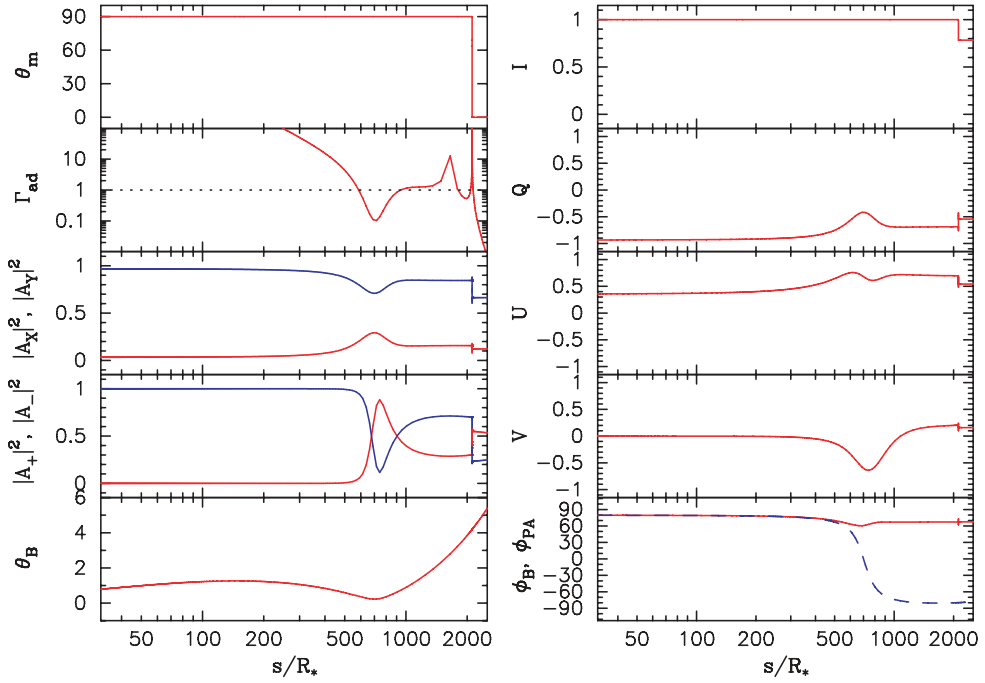

Figure 7. Same as Fig. 6, except for the impact angle $\chi = 0.^{\circ}5$. The very smaller impact angle makes ϕ_B change more quickly around $s \sim 700R_*$ so that the QT effect is stronger than the case shown in Fig. 6. Note that the sign of final CP is different from the cases in Figs 4 and 6.

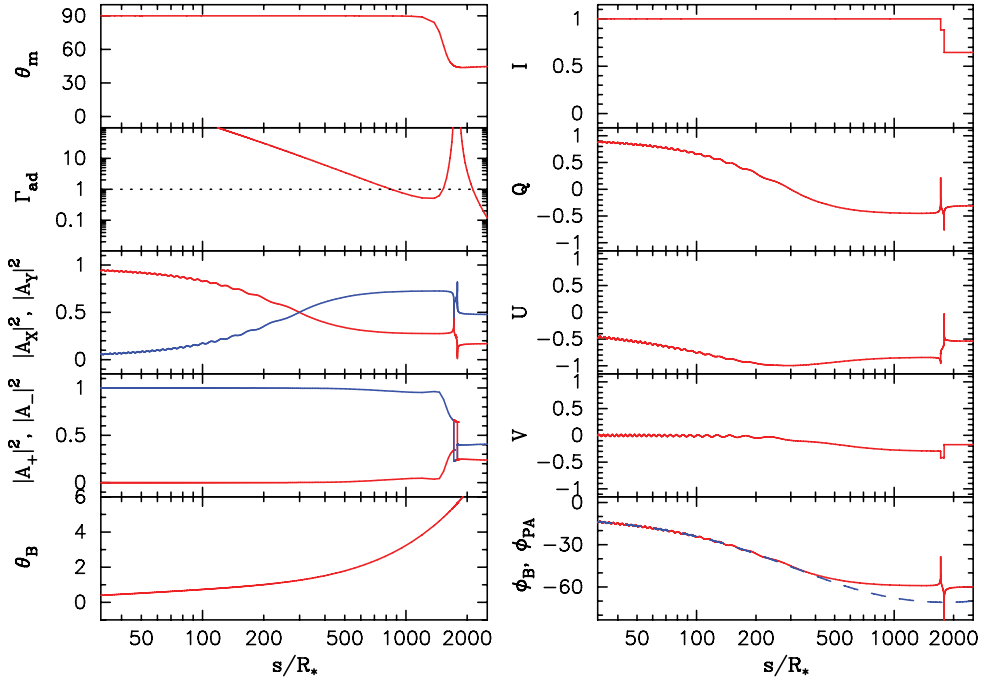

Figure 8. Same as Fig. 4, except for an asymmetric pair plasma with $\Delta\gamma/\gamma = 0.2$, $\Delta N/N = 0$. Since the Lorentz factors of electrons and positrons are different, their cyclotron resonance occurs at different radii. Note that after the cyclotron resonance, the natural modes become circular polarized ($\theta_{\rm m} = 45^{\circ}$).

This emission point, $\boldsymbol{r}_{\rm i} = (r_{\rm em}, \theta_{\rm ri}, \phi_{\rm ri})$, is given by (in the fixed *XYZ* frame)

$$\theta_{\rm ri} = \frac{\theta_{\mu i}}{2} - \frac{1}{2}\sin^{-1}\left(\frac{1}{3}\sin\theta_{\mu i}\right), \quad \phi_{\rm ri} = \phi_{\mu i}, \tag{5.83}$$

where $(\theta_{\mu i}, \phi_{\mu i})$ is the initial direction of the dipole magnetic momentum $\boldsymbol{\mu}_i$ and can be found in equation (2.5) (with Ψ given by $\Psi_{\rm i}$). We consider emissions only from the open field line region, i.e. the angle between $\boldsymbol{r}_{\rm i}$ and $\boldsymbol{\mu}_{\rm i}$ should be less than $\sqrt{r_{\rm em}/r_{\rm lc}}$.

For given $r_{\rm em}$, α, ζ, $\Psi_{\rm i}$ and initial polarization state (ordinary mode), we determine $\boldsymbol{r}_{\rm i}$ and calculate the final observed Stokes parameters by integrating along the ray. When the phase $\Psi_{\rm i}$ varies due to NS rotation, we can observe photons from different emission points and the

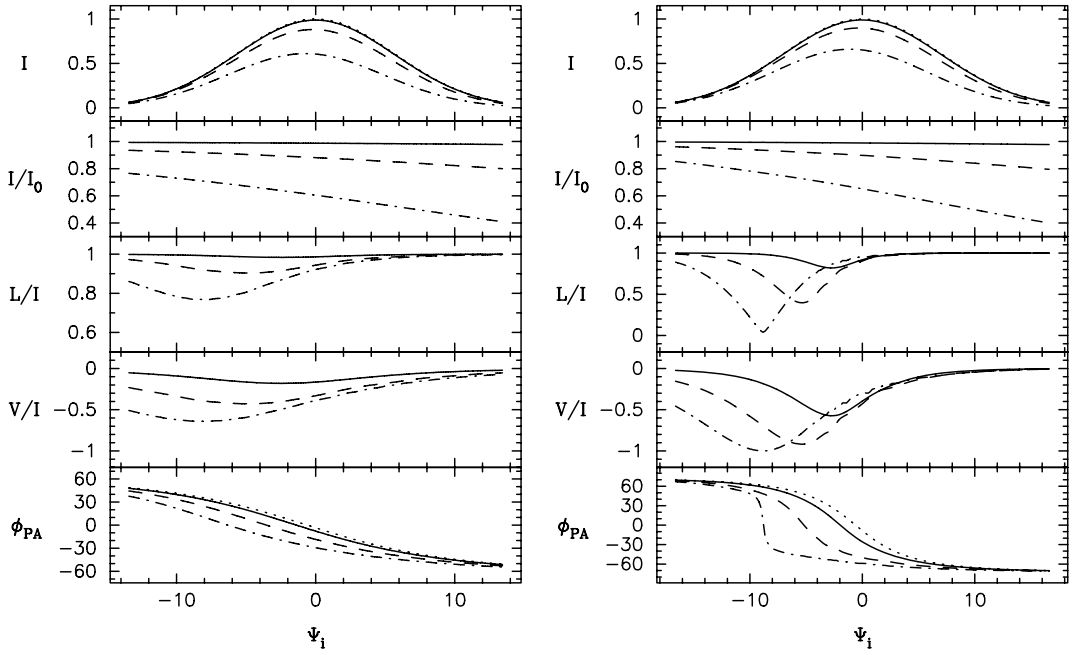

Figure 9. The intensity and polarization profiles computed by ray integrations. We use two different impact angles: (a) $\chi = 5^\circ$ on the left-hand panels and (b) $\chi = 2^\circ$ on the right-hand panels. The solid lines are for the plasma density parameter $\eta = 10$, the dashed lines for $\eta = 100$ and the dot–dashed line for $\eta = 400$. The top panels show the total intensity profiles, where we have adopted (for an illustrative purpose) a Gaussian initial intensity profile $I_0(\Psi_i) = \exp(-4\sqrt{\ln 2}\Psi_i^2/\Psi_{\rm max}^2)$ (this initial profile is shown as dotted lines, almost coincident with the solid lines). The second panels from the top show the modification factor I/I_0 due to propagation effects. The bottom three panels show the LP fraction L/I, CP V/I and the PA of the LP, $\phi_{\rm PA}$. In the bottom panels, the dotted lines (almost coincident with the solid line on the left-hand panel) show the prediction from the RVM: $\phi_{\rm PA} = \phi_{\mu i} \simeq \phi_{Bi}$. In these calculations, the initial polarization states are all of an ordinary mode and the other parameters are the surface magnetic field $B_* = 10^{12}$ G, NS spin period $P = 1$ s, wave frequency $\nu = 1$ GHz, Lorentz factor $\gamma = 100$ (with $\Delta\gamma/\gamma \simeq 0$), inclination angle $\alpha = 30^\circ$ and emission height $r_{\rm em} = 50R_*$.

final observed Stokes parameters will change with the rotation phase – this is the pulsar polarization profile. If we neglect the propagation effect, the observed PA, $\phi_{\rm PA}$, can be described by the RVM (see Radhakrishnan & Cooke 1969) as

$$\phi_{\rm PA} = \phi_{\mu i} = \phi_\mu(\Psi_i) = \tan^{-1}\frac{-\sin\alpha\sin\Psi_i}{\sin\zeta\cos\alpha - \cos\zeta\sin\alpha\cos\Psi_i}. \tag{5.84}$$

The basic assumption of the RVM is that the radiation is emitted with polarization in the plane of the field line curvature (i.e. the $\boldsymbol{k}$–$\boldsymbol{B}$ plane) and this polarization direction is unchanged during the propagation. However, as seen in Section 5.1, the final polarization state can be modified compared to the initial one because of the propagation effect in the magnetosphere so that the final PA profile can deviate significantly from the RVM.

Fig. 9 shows a typical example of the phase evolution of the intensity and polarization, taking into account all the propagation effects. The total intensity is only affected by cyclotron absorption, and a higher plasma density leads to stronger absorption. We see that the relative intensity I/I_0 varies with the rotation phase Ψ_i, simply because the wave passes through different paths in the magnetosphere for different Ψ_i. For illustrative purpose, we consider the initial intensity profile I_0, given by a Gaussian centred at $\Psi_i = 0$:

$$I_0(\Psi_i) = \exp(-4\sqrt{\ln 2}\Psi_i^2/(\Psi_{\rm max}^2)). \tag{5.85}$$

Here $\Psi_{\rm max}$ is the initial phase of the photon from the edge of the open field region and is given by

$$\cos\Psi_{\rm max} = \frac{\cos\theta_{\rm open} - \cos\zeta\cos\alpha}{\sin\zeta\sin\alpha}, \tag{5.86}$$

where $\theta_{\rm open} \simeq \sqrt{r_{\rm em}/r_{\rm lc}}$ is the half-cone angle of the open field region at emission height $r_{\rm em}$ (here we simply assume that the open field region is always the same as the $\boldsymbol{\mu\phi} \parallel \boldsymbol{\Omega}$ case). Since I/I_0 depends asymmetrically on Ψ_i, the observed intensity I is no longer a Gaussian. Non-Gaussian profiles have been observed in many pulsars, and the phase-dependent cyclotron absorption illustrated here is a possible explanation.

The final polarization profiles are also strongly affected by the propagation effects. When the plasma density is not so high and/or the impact angle χ is not so small (compared to the half-cone angle of the emission beam from the open field region $\theta_{\rm beam}$; e.g. in Fig. 9a, $\chi = 5^\circ$ while $\theta_{\rm beam} \simeq 1.5\theta_{\rm open} = 8.^\circ 8$), the wave mode coupling effect is not strong and the final CP is not very high. In this case, the final LP PA is determined by the azimuthal angle of the $\boldsymbol{B}$ field at the polarization limiting radius $\phi_B(r_{\rm pl})$:

$$\phi_{\rm PA} \simeq \phi_B(r_{\rm pl}) \simeq \pi + \phi_\mu(r_{\rm pl}) = \pi + \phi_\mu(\Psi_i + r_{\rm pl}/r_{\rm lc}). \tag{5.87}$$

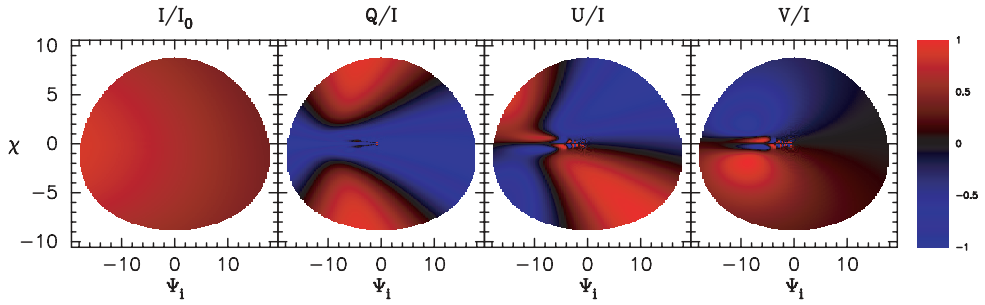

Figure 10. Two-dimensional polarization map of the pulsar emission beam. The four panels correspond to the four Stokes parameters I, Q/I, U/I, V/I. The filled region is the emission beam from the open field region. The values of the four Stokes parameters are shown with different colours (with red for a positive value while blue for negative). The map is obtained by computing the observed wave polarization for different impact angles χ (which varies from $-\theta_{\rm beam}$ to $\theta_{\rm beam}$; here $\theta_{\rm beam} \simeq 8.^{\circ}8$) and the rotation phase $\Psi_{\rm i}$. The other (fixed) parameters are the surface magnetic field $B_* = 10^{12}$ G, NS period $P = 1$ s, wave frequency $\nu = 1$ GHz, plasma density $\eta = N/N_{\rm GJ} = 400$ ($N = N_{\rm e} + N_{\rm p}$ and $N_{\rm e} = N_{\rm p}$), Lorentz factor $\gamma = 100$ (with $\Delta\gamma/\gamma \simeq 0$), inclination angle $\alpha = 30^{\circ}$ and emission height $r_{\rm em} = 50R_*$.

Here we have used the approximation of $\boldsymbol{B}(\boldsymbol{r}) = -\boldsymbol{\mu}/r^3$ since $r_{\rm pl} \gg R_*$. In general, the polarization limiting radius, $r_{\rm pl}$, does not vary significantly with different rotation phases $\Psi_{\rm i}$. Thus, the final PA profile just shifts by the amount

$$r_{\rm pl}/r_{\rm lc} \simeq 0.04 \left(\frac{\eta}{10^2}\right)^{1/3} \left(\frac{B}{10^{12}\,{\rm G}}\right)^{1/3} \left(\frac{\nu}{1\,{\rm GHz}}\right)^{-1/3} \left(\frac{\gamma}{10^2}\right)^{-1} \left(\frac{\theta_B}{0.1}\right)^{-2/3} \left(\frac{P}{1\,{\rm s}}\right)^{-1} \left(\frac{F_\phi}{10}\right)^{-1/3} \tag{5.88}$$

compared to the RVM. The final CP is always a single sign in this case. We can easily find the relationship between $\phi_{\rm PA}$ and the sign of CP. According to equation (5.87), the monotonicity of the final PA, $\phi_{\rm PA}(\Psi_{\rm i})$, is given by

$$\frac{{\rm d}\phi_{\rm PA}}{{\rm d}\Psi_{\rm i}} = \frac{{\rm d}\phi_B(r_{\rm pl})}{{\rm d}\Psi}\frac{{\rm d}\Psi}{{\rm d}\Psi_{\rm i}} = \frac{{\rm d}\phi_B(r_{\rm pl})}{{\rm d}\Psi}. \tag{5.89}$$

Here $\Psi = \Psi_{\rm i} + s/r_{\rm lc}$ (see equation 2.2) so that ${\rm d}\Psi/{\rm d}\Psi_{\rm i} = 1$. The sign of the final CP (generated by the wave mode coupling effect) is determined by ${\rm d}\phi_B(r_{\rm pl})/{\rm d}s$ (ϕ_B' in equation 4.77), and

$$\frac{{\rm d}\phi_B(r_{\rm pl})}{{\rm d}s} = \frac{{\rm d}\phi_B(r_{\rm pl})}{{\rm d}\Psi}\frac{{\rm d}\Psi}{{\rm d}s} = \frac{{\rm d}\phi_B(r_{\rm pl})}{{\rm d}\Psi}\frac{1}{r_{\rm lc}} \tag{5.90}$$

so that ${\rm d}\phi_{\rm PA}/{\rm d}\Psi_{\rm i}$ always has the same sign as ${\rm d}\phi_B(r_{\rm pl})/{\rm d}s$. According to equations (4.77) and (5.90), we can find that because of the wave mode coupling effect, a monotonically increasing $\phi_{\rm PA}$ leads to a positive V while a monotonically decreasing $\phi_{\rm PA}$ gives a negative V. This relationship has been observed in some conal-double-type pulsars (see Section 5.3).

The polarization profiles can also be quite different from the RVM prediction, especially in the case of low impact angle and/or high plasma density. Fig. 9(b) give some examples for the impact angle $\chi = 2^{\circ}$. For the low density case of $\eta = 10$, the final PA profile can still be approximated by a simple shift from the RVM. However, for higher density ($\eta = 200$, 400), the final PA profile is not just a simple shift compared with the RVM. For example, the PA profile of the $\eta = 400$ case has a 90° jump within 1° around $\Psi_{\rm i} \simeq -9^{\circ}$, where the LP L/I is close to 0 while the CP $|V|/I$ reaches almost 100 per cent. In this region, the QT effect (discussed in Section 4.4) plays an important role in determining the final polarization state (see Fig. 6).

5.3 Two-dimensional polarization maps of the pulsar emission beam

For a given pulsar, observation at a different line of sight (i.e. different ζ or impact angle χ) would obviously result in different intensity and polarization profiles. Fig. 10 gives an example of the two-dimensional polarization map of the observed Stokes parameters, produced by varying χ and $\Psi_{\rm i}$, while keeping all other parameters fixed. As discussed before, the final total intensity I is only affected by cyclotron absorption, while the linear and CPs are modified by wave mode coupling effect and QT effect, and can deviate significantly from the prediction of the RVM. Fig. 11 shows four profiles with four different impact angles χ, corresponding to four sections of Fig. 10. These four sections represent the following three typical final polarization states produced by the propagation effects.

(i) For a relatively large impact angle $|\chi|$, the final PA profile can be obtained by a small shift from the RVM profile, of the amount $r_{\rm pl}/r_{\rm lc}$ (see equations 5.87 and 5.88). Fig. 9 and the $\chi = -5^{\circ}$ column of Fig. 11 depict some examples. The final CP is always of a single sign: a monotonically increasing $\phi_{\rm PA}$ leads to a positive V while a monotonically decreasing $\phi_{\rm PA}$ gives a negative V (see equations 4.77 and 5.90). This behaviour is consistent with observations of the double cone emission of some pulsars ('conal-double-type pulsars'), where a correlation between the sense of CP and the sense of PA variation was found (see Han et al. 1998).

(ii) For a relatively small impact angle, the final PA profile is very different from the RVM prediction – the middle two columns ($\chi = -1.^{\circ}9$ and $\chi = -1^{\circ}$) of Fig. 11 give some examples. It is clear that there always exists a special line of sight ($\chi = \chi_{\rm jump}$), for which the PA profile has a 90° jump [where $Q = 0$ while U changes signs (see the $\chi = -1.^{\circ}9$ column of Fig. 11)]. The large jumps in V/I and $\phi_{\rm PA}$ are caused by the QT effect. For $|\chi| < \chi_{\rm jump}$, the PA is not necessarily a monotonic function of $\Psi_{\rm i}$. Nevertheless, the final CP retains a single sign, which is the same as the case with large $|\chi|$.

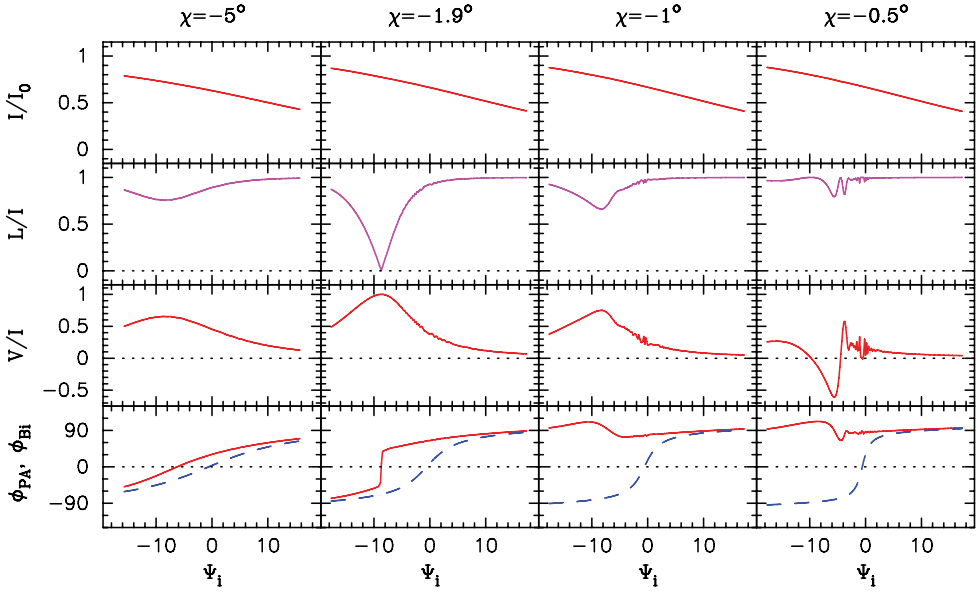

Figure 11. Intensity and polarization profiles of the pulsar emission beam. The four columns correspond to four fixed impact angles $\chi = -5^\circ, -1.^\circ9, -1^\circ$ and $-0.^\circ5$, respectively, which are four sections in Fig. 10. In each column, we plot the Stokes parameters I/I_0 (top panel), L/I (second panel), V/I (third panel), $\phi_{\rm PA}$ and $\phi_{\rm Bi}$ (bottom panel; the solid line is for $\phi_{\rm PA}$ and the dashed line for $\phi_{\rm Bi}$). Note that there exists a 90° jump of $\phi_{\rm PA}$ near $\Psi_{\rm i} = -9^\circ$ in the bottom panel of the $\chi = -1.^\circ9$ column. The other parameters are the same as in Fig. 10.

(iii) For a very small impact angle ($|\chi| \ll \chi_{\rm jump}$), the QT effect is much stronger so that the final PA profile is very different from the prediction of the RVM and even the CP does not stay at a single sign (see the rightmost column of Fig. 11).

The above three types of polarization behaviours always exist for different pulsar and plasma parameters (e.g. B_*, P_0, ν, η, γ, α and $r_{\rm em}$). Different parameters just modify the position of $\chi_{\rm jump}$ and the initial rotation phase where the 90° jump in PA occurs, while the basic morphology of the emission beam does not change.

6 CONCLUSION AND DISCUSSION

We have studied the evolution of radio emission polarization in a rotating pulsar magnetosphere filled with a relativistic streaming pair plasma. We quantify and compare the relative importance of several key propagation effects that can influence the observed radio polarization signals, including wave mode coupling, cyclotron absorption, propagation through the QT region and mode circularization (due to asymmetric distributions of electrons and positrons). We use numerical integration of the photon polarization along the ray to incorporate all these propagation effects self-consistently within a single framework. We find that, for typical parameters of the magnetospheric plasma produced by pair cascade, and for an initially 100 per cent linear-polarized radio wave, the final intensity and polarization PA are modified by the propagation effects, and significant CP can be generated.

We find that the most important propagation effects are cyclotron absorption, wave mode coupling and QT effect. Generally, cyclotron absorption occurs after the wave mode coupling ($r_{\rm cyc} > r_{\rm pl}$; see equation 4.73). Thus, it only changes the total wave intensity and does not modify the wave polarization ($\phi_{\rm PA}$, V/I). For a large impact angle $|\chi|$ and/or relatively low plasma density, the final wave polarization angle $\phi_{\rm PA}$ is determined by the azimuthal angle of the $\boldsymbol{B}$ field at the polarization limiting radius $r_{\rm pl}$, and the observed CP is determined by the value of $\Lambda = r_{\rm pl}\,\phi'_B$ at $r = r_{\rm pl}$ (see equations 4.76 and 4.77). In this case, the observed $\phi_{\rm PA}$ profile is similar to the prediction of the RVM, except for a phase shift by the amount $r_{\rm pl}/r_{\rm lc}$ (see equation 5.88); the CP has a single sign across the emission beam (see Fig. 9). For a small impact angle and/or high plasma density, the QT effect becomes important; the final polarization profiles are more irregular: a 90° sudden jump in PA may occur at a certain phase, accompanied by large CP. For very small $|\chi|$, the CP may change signs at different phases (see the rightmost column of Fig. 11).

In this paper, we have adopted the simplest (and minimum) assumptions about the property of the magnetospheric plasma and the intrinsic radio emission mechanism (see below). Nevertheless, our results already show great promise in explaining a number of otherwise puzzling observations as follows.

(i) It has been observed that in some single-pulse pulsars, the intensity profile deviates from the single Gaussian shape. One possible reason is that cyclotron absorption depends on the rotation phase (because the ray passes through different regions of the magnetosphere), as discussed in Section 5.2. Thus, even when the initial intensity profile from the emission beam is a Gaussian, the observed profile can be non-Gaussian.

(ii) For the so-called conal-double-type pulsars, which in our model corresponds to a large impact angle χ, the relationship between the single sign of the CP and the derivation of $\phi_{\rm PA}$ (see Han et al. 1998) can be easily understood by the wave mode coupling effect. According to

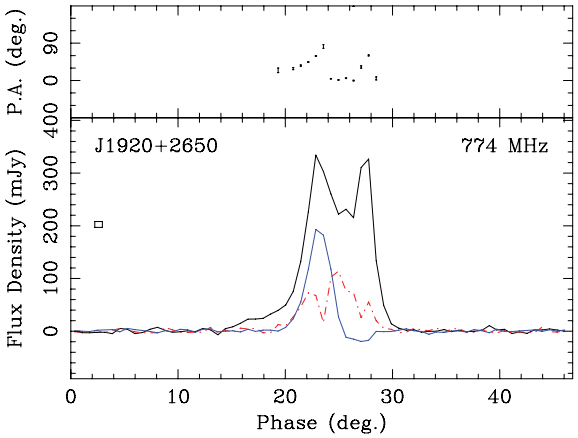

Figure 12. Intensity and polarization profiles of PSR J1920+2650. In the lower panel, the upper thick line is the total intensity (I), the dash–dot–dashed line is the linearly polarized intensity L and the thin line is the circularly polarized intensity V. This pulsar shows extremely strong CP with $V/I \simeq 64$ per cent in its first major component.

equations (4.77) and (5.90), an increasing $\phi_{\rm PA}$ corresponds to the right-hand CP ($V > 0$) while a decreasing $\phi_{\rm PA}$ corresponds to the left-hand ($V < 0$) one.[2]

(iii) According to our calculation, there exists a special impact angle $\chi_{\rm jump}$, where the observed $\phi_{\rm PA}$ profile has a 90° jump (OPM) and this is accompanied by the maximum CP. This feature may be helpful to explain the polarization profile of PSR J1920+2650 (Fig. 12; see Han et al. 2009).

(iv) For a very small impact angle, which corresponds to the core emission, the QT effect can cause the sign reversal of CP, which is observed in the core components of many pulsars (e.g. Radhakrishnan & Rankin 1990; Han et al. 1998; You & Han 2006).

Our calculations in this paper have relied on several simplifying assumptions. For example, we have assumed that the radio emission is from the same height for different rotation phases, that the density parameter ($\eta = N/N_{\rm GJ}$) of the magnetospheric plasma is constant everywhere in the emission cone and along the photon trajectory, and that the plasma electrons and positrons are the same for bulk Lorentz factors. In future works, we plan to consider models with varying emission heights as well as non-trivial electron/positron spatial and velocity distributions. We did not include the small but finite emission cone (angle $1/\gamma$) in our model and assumed that the initial polarization of a photon is always O mode for different rotation phases. However, different emission mechanisms could give different initial polarization states. We will also be interested in studying the propagation effects on the individual/subpulse emissions, since they may more directly reflect the underlying radio emission processes.

ACKNOWLEDGMENTS

This work has been supported in part by NASA grant NNX07AG81G and NSF grant AST 0707628. Authors are also supported by the National Natural Science Foundation of China (10773016, 10821001 and 10833003) and the Initialization Fund for President Award winner of Chinese Academy of Sciences.

REFERENCES

Allen M. C., Melrose D. B., 1982, Proc. Astron. Soc. Australia, 4, 365
Arons J., Barnard J. J., 1986, ApJ, 302, 120
Backer D. C., Rankin J. M., Campbell D. B., 1976, Nat, 263, 202
Barnard J. J., 1986, ApJ, 303, 280
Barnard J. J., Arons J., 1986, ApJ, 302, 138
Beloborodov A. M., Thompson C., 2007, ApJ, 657, 967
Blaskiewicz M., Cordes J. M., Wasserman I., 1991, ApJ, 370, 643
Cheng A. F., Ruderman M. A., 1979, ApJ, 229, 348
Cognard I., Shrauner J. A., Taylor J. H., Thorsett S. E., 1996, ApJ, 457, 81
Cordes J. M., 1978, ApJ, 222, 1006
Cordes J. M., Rankin J., Backer D. C., 1978, ApJ, 223, 961
Daugherty J. K., Harding A. K., 1982, ApJ, 252, 337
Fussell D., Luo Q., Melrose D. B., 2003, MNRAS, 343, 1248
Gangadhara R. T., 1997, A&A, 327, 155

[2] Here we define the sign of CP in the fixed XYZ-frame (see Fig. 1) using equation (2.12), which is a little bit different from the definition in electrical engineering used by Han et al. (1998).

Gould D. M., Lyne A. G., 1998, MNRAS, 301, 235
Han J. L., Demorest P. B., van Straten W., Lyne A. G., 2009, ApJS, 181, 557
Han J. L., Manchester R. N., Xu R. X., Qiao G. J., 1998, MNRAS, 300, 373
Hibschman J. A., Arons J., 2001, ApJ, 554, 624
Johnston S., Ball L., Wang N., Manchester R. N., 2005, MNRAS, 358, 1069
Kazbegi A. Z., Machabeli G. Z., Melikidze G. I., 1991, MNRAS, 253, 377
Kijak J., Gil J., 2003, A&A, 397, 969
Kramer M., Xilouris K. M., Jessner A., Lorimer D. R., Wielebinski R., Lyne A. G., 1997, A&A, 322, 846
Lai D., Ho W. C. G., 2002, ApJ, 566, 373
Lai D., Ho W. C. G., 2003, ApJ, 588, 962
Luo Q. H., Melrose D. B., 2001, MNRAS, 325, 187
Luo Q. H., Melrose D. B., 2004, in Camilo F., Gaensler B. M., eds, Proc. IAU Symp. 218, Young Neutron Stars and Their Environments. Astron. Soc. Pac., San Francisco, p. 381
Lyne A. G., Manchester R. N., 1988, MNRAS, 234, 477
Lyubarsky Y., 2008, in Bassa C., Wang Z., Cumming A., Kaspi V. M., eds, AIP Conf. Ser. Vol. 983, 40 Years of Pulsars: Millisecond Pulsars, Magnetars and More. Am. Inst. Phys., New York, p. 29
Lyubarskii Y. E., Petrova S. A., 1998, Ap&SS, 262, 379
McKinnon M. M., Stinebring D. R., 2000, ApJ, 529, 435
Manchester R. N., Taylor J. H., Huguenin G. R., 1975, ApJ, 196, 83
Medin Z., Lai D. 2010, MNRAS, submitted (arXiv:1001.2365)
Melrose D. B., 2003, in Bailes M., Nice D. J., Thorsett S. E., eds, ASP Conf. Ser. Vol. 302, Radio Pulsars. Astron. Soc. Pac., San Francisco, p. 179
Melrose D. B., 1979, Australian J. Phys., 32, 61
Mitra D., Li X. H., 2004, A&A, 421, 215
Petrova S. A., 2006, MNRAS, 366, 1539
Petrova S. A., Lyubarskii Y. E., 2000, A&A, 355, 1168
Radhakrishnan V., Cooke D. J., 1969, ApJ, 3, 225
Radhakrishnan V., Rankin J. M., 1990, ApJ, 352, 258
Rafikov R. R., Goldreich P., 2005, ApJ, 631, 488
Rankin J. M., 1983, ApJ, 274, 333
Stinebring D. R., Cordes J. M., Rankin J. M., Weisberg J. M., Boriakoff V., 1984a, ApJS, 55, 247
Stinebring D. R., Cordes J. M., Weisberg J. M., Rankin J. M., Boriakoff V., 1984b, ApJS, 55, 279
Thompson C., Lyutikov M., Kulkarni S. R., 2002, ApJ, 574, 332
van Adelsberg M., Lai D., 2006, MNRAS, 373, 1495
von Hoensbroech A., Lesch H., Kunzl T., 1998, A&A, 336, 209
Wang C., Lai D., 2007, MNRAS, 377, 1095
Wang C., Lai D., 2009, MNRAS, 398, 515
Weisberg J. M. et al., 1999, ApJS, 121, 171
Weisberg J. M., Cordes J. M., Kuan B., Devine K. E., Green J. T., Backer D. C., 2004, ApJS, 150, 317
Xilouris K. M., Seiradakis J. H., Gil J., Sieber W., Wielebinski R., 1995, A&A, 293, 153
Xu R. X., Liu J. F., Han J. L., Qiao G. J., 2000, ApJ, 535, 354
You X. P., Han J. L., 2006, Chinese J. Astron. Astrophys., 6, 237

This paper has been typeset from a TEX/LATEX file prepared by the author.